FUNCTIONAL PHOTOACOUSTIC TOMOGRAPHY OF ANIMAL BRAINS

A Dissertation

by

XUEDING WANG

Submitted to the Office of Graduate Studies of
Texas A&M University
in partial fulfillment of the requirements for the degree of

DOCTOR OF PHILOSOPHY

August 2004

Major Subject: Biomedical Engineering

FUNCTIONAL PHOTOACOUSTIC TOMOGRAPHY OF ANIMAL BRAINS

A Dissertation

by

XUEDING WANG

Submitted to the Office of Graduate Studies of
Texas A&M University
in partial fulfillment of the requirements for the degree of

DOCTOR OF PHILOSOPHY

Approved as to style and content by:

Lihong V. Wang (Chair of Committee)	Gerard L. Coté (Member)
Hsin-i Wu (Member)	Gheorghe Stoica (Member)
William Hyman (Head of Department)	

August 2004

Major Subject: Biomedical Engineering

ABSTRACT

Functional Photoacoustic Tomography of Animal Brains. (August 2004)

Xueding Wang, B.S., Nanjing University;
M.S., Nanjing University
Chair of Advisory Committee: Dr. Lihong V. Wang

This research is primarily focused on laser-based non-invasive photoacoustic tomography of small animal brains. Photoacoustic tomography, a novel imaging modality, was applied to visualize the distribution of optical absorptions in small-animal brains through the skin and skull. This technique combines the high-contrast advantage of optical imaging with the high-resolution advantage of ultrasonic imaging. Based on the intrinsic optical contrast, this imaging system successfully visualized three-dimensional tissue structures in intact brains, including lesions and tumors in brain cerebral cortex. Physiological changes and functional activities in brains, including cerebral blood volume and blood oxygenation in addition to anatomical information, were also satisfactorily monitored. This technique successfully imaged the dynamic distributions of exogenous contrast agents in small-animal brains. Photoacoustic angiography in small-animal brains yielding high contrast and high spatial resolution was implemented non-invasively using intravenously injected absorbing dyes. In the appendix, the theory of Monte Carlo simulation of polarized light propagation in scattering media was briefly summarized.

DEDICATION

To my wife, my parents and my parents in law

who have always been supportive with love and understanding.

ACKNOWLEDGEMENTS

It has been my great pleasure to work in the Optical Imaging Laboratory at Texas A&M University for the past four years, which have been the most rewarding experience in my life. I would like to thank Dr. Lihong Wang for supporting me through his research funding and for providing me this great opportunity to study in his lab. His broad knowledge and acute insight guided me all through this research. As an advisor, Dr. Wang tried his best to advance his students and gave us plenty of opportunities to communicate with researchers in this field at many professional conferences. Without his valuable assistance, I would never have been able to publish papers in highly ranked journals.

I'd like to thank Dr. George Stoica who continuously supported my animal experiments. He has taught me knowledge in biological areas without reservation and has opened the door of neurophysiology for me to explore. He is indispensable to my successful completion of this research project.

I also owe many thanks to Dr. Coté who has encouraged me throughout my research and has given me valuable suggestions to my career development.

Last but not least, I would like to thank Geng Ku, Xueyi Xie, Yongjiang Pang, Yiwen Wang, Minghua Xu, Yuan Xu, Dazhi Feng, and all members in the Optical Imaging Laboratory for their assistance and contribution to my work.

TABLE OF CONTENTS

CHAPTER Page

LIST OF FIGURES

FIGURE Page

CHAPTER I

INTRODUCTION

With many intrinsic advantages, such as non-ionization, high sensitivity and low cost, optical techniques for functional imaging and therapeutic monitoring of biological samples are highly desirable. High contrasts related to the optical properties of biological tissues in visible or near-infrared (NIR) region of electromagnetic spectrum can be used in describing tissue structures and disorders, deducing functional parameters in living tissues, and studying functional cellular and biochemical information. The absorption contrast between the blood and the surrounding medium is around 1000% for 850-nm light.[1] The absorption contrast between tumors and[1] surrounding normal tissues can be as high as 300% for NIR light[2] and even higher in the visible region due to the large blood content in malignant tissues. Optical properties can be used to quantify the hallmarks of cancers, including angiogenesis, hyper-metabolism and pleomorphism, and hence can enable the detection and study of early cancers. Spectroscopic differences between oxy- and deoxy-hemoglobin can be used to deduce physiological parameters such as hemoglobin oxygen saturation (blood oxygenation) and total concentration of hemoglobin (blood volume).[3,4] Optical scattering properties of tissues are related to the morphologies and refractive indices of tissue compositions, such as cells, nucleus and other scattering particles.[5–7] Therefore, the scattering properties of tissues can be used to monitor architectural changes at the cellular and sub-cellular levels. Furthermore, by employing exogenous bioactive optical contrast agents, optical imaging can reveal functional information of living tissues at the molecular or genetic level.

The major challenge faced by optical imaging is the overwhelming scattering of light in biological tissues. Most biological tissues, except ocular tissue, have high scattering coefficients ranging from 10 cm^{-1} to >100 cm^{-1} for light transport. After propagating several millimeters in biological tissues, most photons will be scattered many times and hence randomly distributed. The difficulty in keeping the trajectory and state of the light in tissues makes optical imaging harder to apply than some other imaging

This dissertation follows the style and format of Applied Optics.

techniques such as ultrasonic imaging and x-ray imaging.

In the past decade, many imaging modalities based on optical contrast have been proposed and developed. Confocal microscopy,[8,9] optical-coherence tomography (OCT)[10,11] and ultrafast time gating optical imaging[12,13] are all based on pure optical signals provided by ballistic photons. These imaging modalities can achieve satisfactory imaging resolutions but cannot enable imaging of deep tissues. Another pure optical imaging modality—diffusion optical tomography (DOT)—can achieve a satisfactory imaging depth and provide functional information such as the blood oxygenation and blood volume. However, due to the high scattering of light in tissues, the spatial resolution of DOT degrades greatly as the imaging depth increases.

Imaging modalities combining optical techniques with ultrasonic techniques provide another way to realize high-resolution deep imaging of optical properties of biological tissues. For example, photoacoustic tomography[1,14-20] (PAT) and ultrasound-modulated optical tomography[21,22] are two of these hybrid optical imaging techniques that have been explored in the past decade. Compared to electromagnetic waves, the scattering of ultrasonic waves in biological tissues is much weaker. Therefore, the ultrasonic signals are more suitable for deep tissue imaging with satisfactory spatial resolution. In these hybrid imaging techniques, the contrast is provided by the optical properties of biological tissues while the resolution is determined by the ultrasonic signals. In other words, these techniques combine the high-contrast advantage of optical imaging while also utilizing the high-resolution advantage of ultrasonic imaging.

PAT (also referred to as optoacoustic tomography or thermoacoustic tomography) is a non-invasive, nonionizing imaging modality based upon different absorptions of electromagnetic waves for various biological tissues. In PAT, an electromagnetic wave in the visible or NIR region irradiates a biological sample under study. Then photoacoustic waves will be generated in the sample according to the thermoelastic mechanism, which can be detected by highly sensitive piezoelectric devices outside the sample. With the detected photoacoustic signals, the distribution of electromagnetic absorptions in the sample can be reconstructed. PAT technique visualizes the high optical contrast of biological tissues instead of the low acoustic contrast; while its spatial resolution is determined primarily by the bandwidth of photoacoustic signals rather than by the optical

diffusion as in optical imaging.[23] As a result, the imaging depth of PAT is satisfactory. Furthermore, PAT is free of the speckle artifacts presented in OCT and ultrasonography, because photoacoustic waves travel only one way to reach the ultrasonic detector rather than two ways as in OCT and ultrasonography.

The photoacoustic method to detect small deeply embedded tumors has been studied by Esenaliev *et al.*[15,24], Oraevsky *et al*.[2] and Andreev *et al*.[25]. In an attempt to advance *in vivo* detection of skin cancer, photoacoustic imaging of layered tissues with optical contrast has been studied by Beenen *et al*.[26], Oraevsky *et al.*[27] and Karabutov *et al*.[28]. Hoelen *et al*.[1] applied photoacoustic technique to image blood vessels 1 cm deep in highly scattering samples and achieved a good axial resolution. Paltauf *et al.*[29] adopted an optical method instead of piezoelectric devices for two-dimensional ultrasonic detection. More recently, Kolkman *et al*.[30] explored *in vivo* photoacoustic imaging of blood vessels in human skin. Fainchtein *et al*.[31] studied photoacoustic measurements on *in vitro* and *in vivo* blood samples and proved that this technique can assess relative changes in the concentrations of oxy- and deoxy-hemoglobin. Single-wavelength photoacoustic detection was employed by Esenaliev *et al*.[32] to monitor the relative change of blood oxygenation *in vitro*.

Various intrinsic optical signals—which are caused mainly by changes in blood volume, oxygen consumption, and cellular swelling[33–37]—have been associated with brain physiology and pathology. This association enables optical contrast to assess physiological and functional properties of brains. Based on intrinsic optical absorptions in biological tissues, PAT provides a non-invasive method to image functional tissue structures and monitor regional oxygen consumption and hemodynamics in brains through skin and skull with satisfactory spatial resolution. As a novel functional imaging modality, functional PAT will greatly accelerate the progress in neurophysiology, neuropathology, and neurotherapy.

In this study, we explored the photoacoustic technique for small-animal brain imaging. Firstly, a PAT system was designed and developed. This system was tested on tissue phantoms and isolated animal organs. Then, we explored the feasibility of PAT of small-animal brains *in situ* and *in vivo*. Both two-dimensional and three-dimensional brain imaging have been fulfilled. Detection and visualization of brain lesions and brain

tumors have been realized. After that, functional imaging of small-animal brains has been performed. The capability of this technique in monitoring the functional parameters, including blood volume and blood oxygenation, in small-animal brains has been studied. Finally, based on the photoacoustic imaging of exogenous contrast agents, angiography in animal brains yielding high contrast and high spatial resolution was implemented.

CHAPTER II

PAT SYSTEM

1. Scanning Method and Imaging Reconstruction

In order to produce photoacoustic waves—based on laser-induced thermoelastic expansion[38,39]—in biological tissues efficiently, the laser pulse must be short; in other words, neither static temperature distributions nor slow heating does produce photoacoustic waves. When a biological sample is irradiated by laser pulses, photoacoustic waves (ultrasonic signals) will be generated. Ultrasonic transducer is very sensitive in detecting small vibrations from an object that are caused by weak absorption of optical energy. By scanning with an ultrasonic transducer or using an ultrasonic transducer array, the photoacoustic waves can be detected outside the sample. Finally, the acquired photoacoustic signals will be used to reconstruct the distribution of the optical absorptions in the sample through a certain algorithm.

We are interested in biological tissues with inhomogeneous optical absorption but relatively homogeneous acoustic properties. When the laser pulse is very short, as in our experiments, the time required for thermal diffusion is much greater than the time for the thermoacoustic transition. Consequently, the effect of heat conduction in the thermoacoustic wave equations can be ignored.[38] As described in previous literatures,[38,40] the photoacoustic signal $p(\mathbf{r},t)$ at position $\mathbf{r}$ and time t is related to a heating source $H(\mathbf{r},t)$ by the following wave equation:

$$\nabla^2 p(\mathbf{r},t) - \frac{1}{c_s^2}\frac{\partial^2}{\partial t^2} p(\mathbf{r},t) = -\frac{\beta}{C_p}\frac{\partial H(\mathbf{r},t)}{\partial t} \tag{1}$$

where c_s is the acoustic velocity; β is the isobaric volume expansion coefficient; C_p is the specific heat; $H(\mathbf{r},t)$ is the heating function defined as the optical energy deposited by the irradiation source per time and volume, which can be written as the product of a temporal illumination function and a spatial absorption function: $H(\mathbf{r},t) = I_0 T(t) A(\mathbf{r})$, where I_0 is a factor proportional to the incident optical energy density; $T(t)$ describes the temporal irradiation of the electromagnetic source that can be regarded as a Dirac delta function $\delta(t)$ for a short light pulse; and $A(\mathbf{r})$ describes the spatially distributed optical

energy deposition. Assuming that the laser energy is homogenous in the imaging plane, $A(\mathbf{r})$ describes the distribution of relative optical absorptions in biological tissues at a certain wavelength. The photoacoustic signal $p(\mathbf{r},t)$ can be rewritten as

$$p(\mathbf{r},t)=\frac{I_0\beta}{4\pi C_p}\iiint\frac{d^3r'}{|r-r'|}A(\mathbf{r}')T'(t')\,. \tag{2}$$

Keeping the incident optical energy density and the structure of an absorbing object unchanged, the intensity of the photoacoustic signal produced by this object is proportional to its absorption coefficient.

The objective of image reconstruction in PAT is to estimate the distribution of optical absorptions $A(\mathbf{r})$ in biological tissues from a set of measured photoacoustic signals $p(\mathbf{r},t)$. A modified back-projection algorithm developed recently by our laboratory[23] and the configuration of laser illumination relative to the acoustic detection plane in combination with the full-view detection of the imaging cross-section played a crucial role to achieve a high-quality PAT on brains.

The modified back-projection algorithm is based on the assumption that the distance between the transducer and the sample is much larger than the wavelengths of the photoacoustic waves that are useful for imaging (true in our experiments). In reconstruction, we used 1.5 mm/μs as the estimated acoustic velocity c_s in soft tissues. When an imaged sample has nearly homogeneous acoustic properties, the small difference between the estimated acoustic velocity and actual acoustic velocity will not cause any distortion in the relative location of the absorption distribution in the sample. In other words, the absolute locations and sizes of the detected targets inside the sample may be changed; however, their relative positions will not be altered.

For two-dimensional (2-D) imaging realized through a scan of an ultrasonic transducer (non-focused in the imaging plane) along a circle around an imaging plane (see Fig. 1), the 2-D distribution of optical absorptions in the imaging plane can be reconstructed through the following formula[23]

$$A(\mathbf{r})=-\frac{r_0^2C_p}{2\pi I_0c_s^4\beta}\int_{\theta_0}d\theta_0\frac{1}{t}\frac{\partial p(\mathbf{r}_0,t)}{\partial t}\bigg|_{t=|\mathbf{r}_0-\mathbf{r}|/c_s}, \tag{3}$$

where θ_0 is the angle along the scanning circle.

For three-dimensional (3-D) imaging realized through a scan of an ultrasonic transducer (non-focused) along a cylindrical surface around a sample (see Fig. 2), the 3-D distribution of optical absorptions in the sample can be reconstructed through the following formula[23]

$$A(\mathbf{r}) = -\frac{r_0^2 C_p}{2\pi I_0 {c_s}^4 \beta} \iint_{S_0} dS_0 \frac{1}{t} \frac{\partial p(\mathbf{r}_0, t)}{\partial t}\bigg|_{t=|\mathbf{r}_0-\mathbf{r}|/c_s}, \tag{4}$$

where S_0 is the cylindrical surface of the scanned cylinder.

We have verified the above 2-D and 3-D reconstruction algorithms in photoacoustic imaging experiments on small-animal brains. The brain images reconstructed by the modified back-projection method matched the anatomical photographs very well with satisfactory spatial resolution.

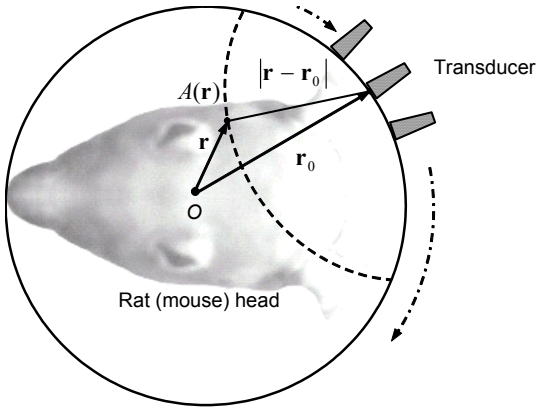

Fig. 1. 2-D circular scan geometry for photoacoustic imaging. The ultrasonic transducer detects the photoacoustic signals along a circle around the imaging plane.

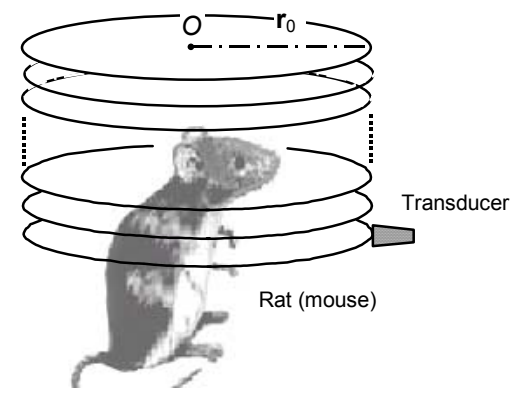

Fig. 2. 3-D cylindrical scan geometry for photoacoustic imaging. The ultrasonic transducer detects the photoacoustic signals along a cylindrical surface around the sample.

2. Experimental Setup

Our PAT system for small-animal brain imaging is shown in Fig. 3, where a laboratory coordinate system (*x, y, z*) is also depicted. A tunable dye laser (ND6000, Continuum) pumped by an Nd:YAG laser (Brilliant B, Bigsky) is employed to provide

laser pulses with a pulse duration of 6.5-ns FWHM and a repetition rate of 10 Hz. The wavelength of the laser light is continuously tunable from 532 nm to 1064 nm. The incident energy density of the laser beam on the surface of the animal head is controlled to be less than the maximum permissible exposure (MPE) according to the ANSI standard.[41] A wide-band ultrasonic transducer is used to detect the photoacoustic signals. The water in the tank couples the photoacoustic signals between the transducer and the animal head. Driven by a computer-controlled step motor, the transducer can scan circularly around the animal head in the horizontal plane (x-y plane). The typical scanning radius is ~3 cm and the scanning step is 1.5°. In most of our imaging experiments on small-animal brains, a circular scan of ~2π angle with ~240 steps is applied. In each scanning step, 50 laser pulses (5 seconds) are used for signal averaging. In this case, a circular scan of photoacoustic signals needs ~25 minutes. Through a translation stage, the transducer can also move along the z-axis to realize a 3-D cylindrical scan. The photoacoustic signals detected by the transducer are received by an amplifier (500 PR, Panametrics) and then sent to an oscilloscope (TDS-640A, Tektronix). Finally, the computer collects the digitized signals to reconstruct the distribution of optical absorptions in the animal brain.

The animal head under imaging is fixed steadily by a homemade animal holder through two ear pins and a breathing mask. The animal head protrudes into the water tank through a hole in the bottom of the tank while a piece of clear membrane between the water and the animal head seals the hole. A thin layer of ultrasonic coupling gel is applied on the surface of the animal head.

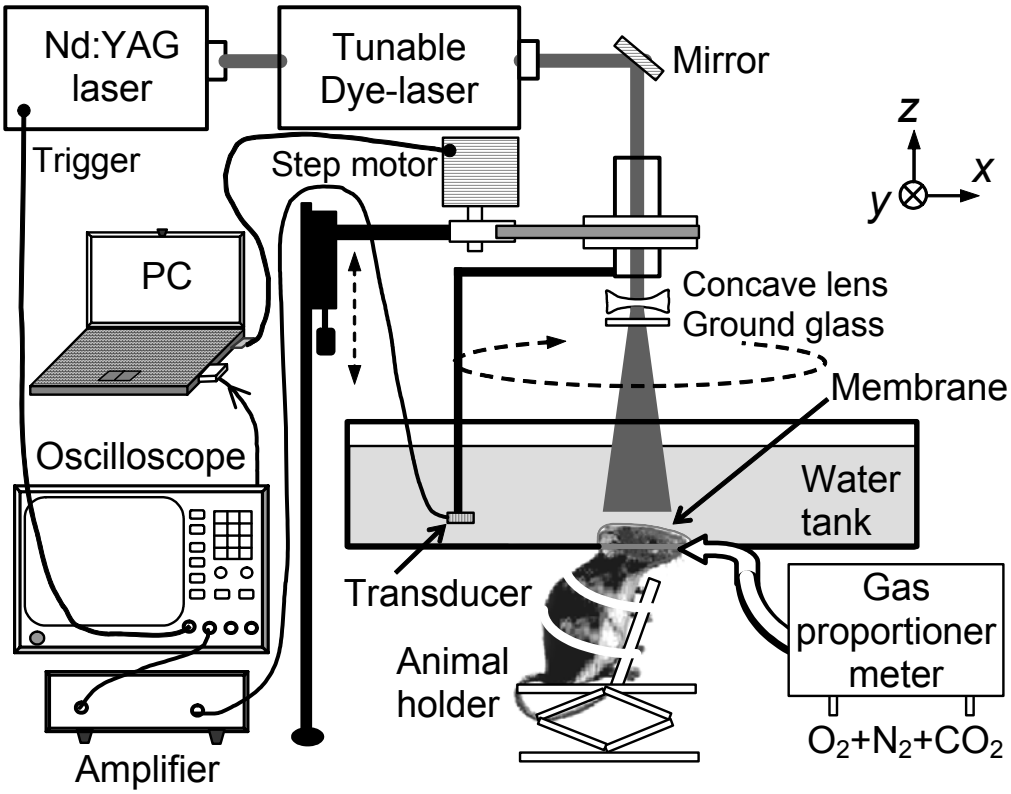

Fig. 3. Schematic of non-invasive PAT system for small-animal brain imaging.

CHAPTER III

PAT BASED ON INTRINSIC CONTRAST

1. Introduction

Optical measurements are classified as either extrinsic or intrinsic. Extrinsic optical signals (or extrinsic optical contrast) are brought by exogenous optical contrast agents; while the intrinsic optical signals (or intrinsic optical contrast) are based on the intrinsic optical properties or physiological events in biological tissues without contrast enhancement. PAT technique can access both the extrinsic and intrinsic optical contrasts by mapping the optical absorptions in biological tissues. Firstly, I will present our study of PAT based on intrinsic optical contrast.

Brain activities are accompanied by certain physiological events, for example, an increase in cerebral blood oxygenation. These events influence certain physiological parameters, for example, the concentrations of oxygenated- and deoxygenated-hemoglobin, that, in turn, can be measured through their influence on optical parameters, for example, light absorption. Oxygenated- and deoxygenated-hemoglobin have characteristic absorption spectra in the visible and NIR regions. Therefore, based on the light absorptions at multiple wavelengths, concentrations of these molecules can be measured.[42-45]

Based on intrinsic optical contrast, functional PAT is promising in imaging brain tissue structures including brain lesions and brain tumors, and monitoring brain functional parameters including brain oxygen consumption and brain hemodynamics. All of these have been fulfilled successfully by our PAT system with high contrast and satisfactory spatial resolution.

2. PAT of *ex vivo* Biological Tissues

In the experiment to test our PAT system, *ex vivo* biological tissues were used. An ultrasonic transducer (V383, Panametrics) with a central frequency of 3.5 MHz and a bandwidth of ~88% at –6 dB was employed as the photoacoustic signal detector. With a cylindrical operating surface and a focal length of ~3.2 cm, the transducer was focused

along the scanning radius (~4 cm) with a focal diameter of ~1 mm and a focal zone of ~3 cm, which determined the spatial resolution along the laser axis but not the resolution in the imaging plane.

Firstly, the experiment was performed with two slices of chicken gizzard tissues placed 0.5 cm deep in a slab of fresh chicken breast. Laser pulses with 789.2-nm wavelength were employed to irradiate the sample. The blood concentration in the chicken gizzard tissue was much higher than that in the chicken breast tissue, and hence, the absorption contrast between them was greater than 200% at the 789.2-nm wavelength according to our measurements.

Fig. 4 shows the photoacoustic image of this sample in comparison with its photograph. It proved that our PAT system as well as the modified back-projection reconstruction algorithm can depict the structures of biological tissues with high contrast and high spatial resolution based on their different optical absorptions.[*,17]

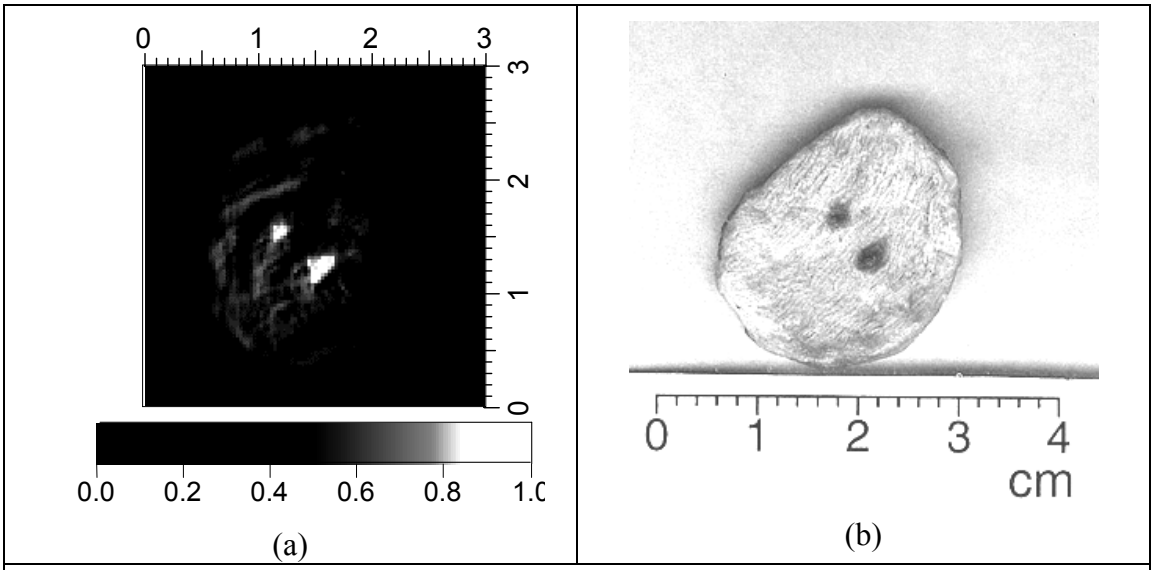

Fig. 4. Photoacoustic imaging of *ex vivo* biological tissues. Two slices of chicken gizzard buried 0.5 cm deep in a slab of chicken breast were imaged. (a) Photoacoustic image, and (b) photograph of the sample.

The PAT system, employing 1064-nm laser light, was also applied to image *ex vivo* rat kidneys. The laser pulse energy was controlled to provide an incident energy

density of ~25 mJ/cm^2 on the kidney surface, which was lower than the ANSI standards for the maximum permissible exposure of pulsed light at the 1064-nm wavelength.

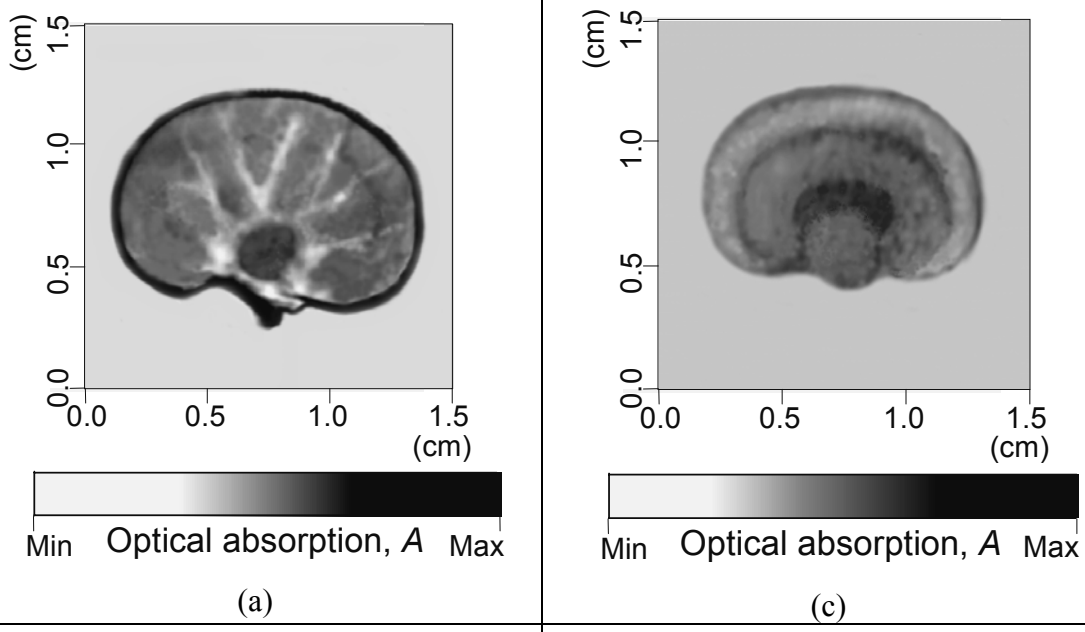

Fig. 5. Photoacoustic imaging of *ex vivo* biological organs. (a) Photoacoustic image and (b) corresponding anatomical photograph of the interior tissue structure of a rat kidney, where the imaged cross-section is ~3 mm beneath the surface. (c) Photoacoustic image and (d) corresponding anatomical photograph of the interior tissue structure of another rat kidney, where the imaged cross-section is ~1 mm beneath the surface.

---

* This material has been published in *Medical Physics* 29, 2799–2805 (2002).

Fig. 5(a) shows the photoacoustic image of the center layer of a rat kidney where the optical absorption is depicted in gray scale (darker areas represent tissues with higher absorptions). The size of the rat kidney is about 1.2 cm×0.8 cm in the imaging plane, and the thickness of the kidney along the *z*-axis is ~0.6 cm. The imaged cross-section is ~0.3 cm below the upper surface of the kidney. By comparing the image and the anatomical photograph [see Fig. 5(b)], we see that the features of the interior tissues, including the renal pelvis and the calyces, are visualized with satisfactory contrast and resolution. Fig. 5(c) shows the photoacoustic image of another rat kidney with similar size, where the imaged cross-section is ~1 mm below the upper surface of the kidney. The image matches well with the interior tissue structures shown by the anatomical photograph [see Fig. 5(d)]. Three layers of soft tissues recognized respectively as the cortex, the cuter medulla and the inner medulla are shown clearly with good contrast.

3. PAT of Small-animal Brains *in situ*

3.1 Photoacoustic imaging of mouse brains in situ

In the experiment of non-invasive photoacoustic imaging of mouse brains *in situ*, 532-nm wavelength was applied. The incident energy density was <10 mJ/cm^2 on the skin of the mouse head, which induced a temperature rise in the skin estimated to be <20 mK. A non-focused ultrasonic transducer (XMS-310, Panametrics) with a center frequency of 10.4 MHz, a bandwidth of ~100% at –6 dB (5.2 MHz–15.6 MHz), and an active element of 2 mm in diameter was used to detect the photoacoustic signals. BALB/c mice (~40 g, Charles River Breeding Laboratories) were employed in this experiment. Hair remover lotion was used to remove the hair on the mouse head. The transducer scanned around the cortical surface of the mouse brain with a scanning radius of 3.1 cm.

Photoacoustic image of a mouse brain achieved non-invasively with the skin and skull intact is shown in Fig. 6(a). The size of the brain is about 1.0 cm×1.5 cm. The optical absorption is depicted in gray scale, where the darker areas—such as the blood vessels—have comparatively higher absorptions. With different optical absorptions, various brain tissues can be identified clearly in the image [see Fig. 6(b)].

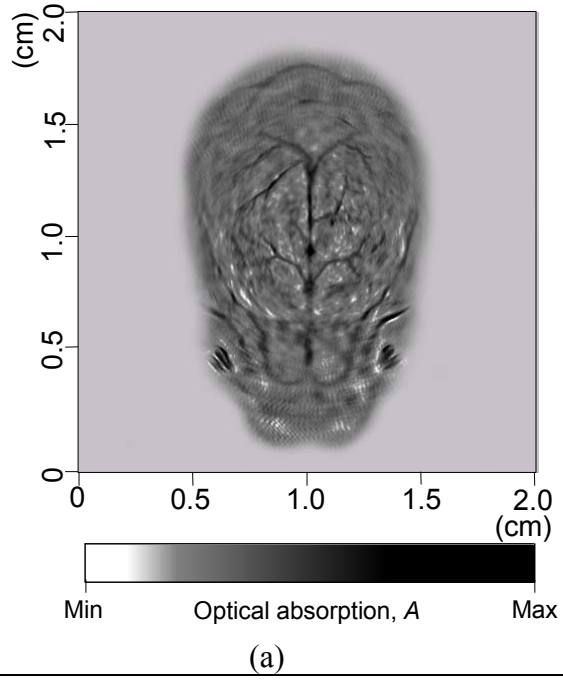

(a)

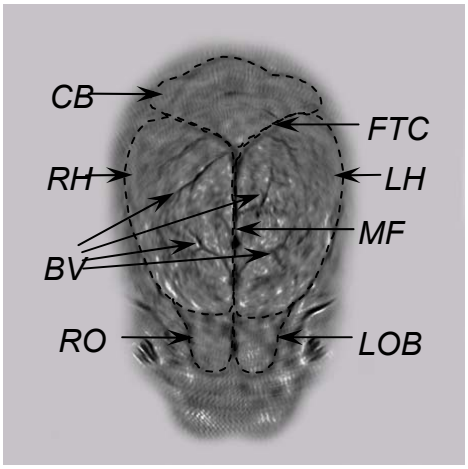

(b)

Fig. 6. Photoacoustic imaging of a mouse brain *in situ*. (a) Image of the mouse brain cerebral cortex achieved non-invasively with the skin and skull intact. Detailed brain tissue structures are indicated in (b): *BV*: blood vessel; *CB*: cerebellum; *FTC*: fissura transversa cerebri; *LH*: left hemisphere; *LOB*; left olfactory lobe; *MF*: median fissure; *RH*: right hemisphere; and *ROB*: right olfactory lobe.

3.2 Photoacoustic imaging of rat brains in situ

In the experiment of non-invasive photoacoustic imaging of rat brains *in situ*, 605-nm wavelength was applied. The incident energy density was <3 mJ/cm^2 on the skin of the mouse head, which induced a temperature rise in the skin estimated to be <6 mK. Adult Sprague Dawley rats (~130 g, Charles River Breeding Laboratories) were imaged by this PAT system. The 10 MHz XMS-310 ultrasonic transducer was used to scan the photoacoustic signals around the rat head with a scanning radius of ~3 cm.

Photoacoustic imaging of the rat brain achieved non-invasively with the skin and skull intact is shown in Fig. 7(a). The optical absorption is depicted in gray scale, where the brighter areas—such as the blood vessels—have comparatively higher absorptions. Due to the absorption contrast between blood and background brain tissues at the 605

nm, the blood vessels in the rat cerebral cortex can be visualized clearly. The imaged vascular structures match well with the open-skull anatomical photography in Fig. 7(b).

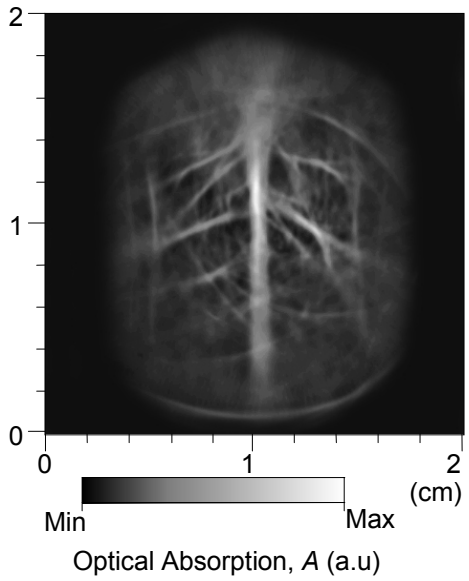

(A)

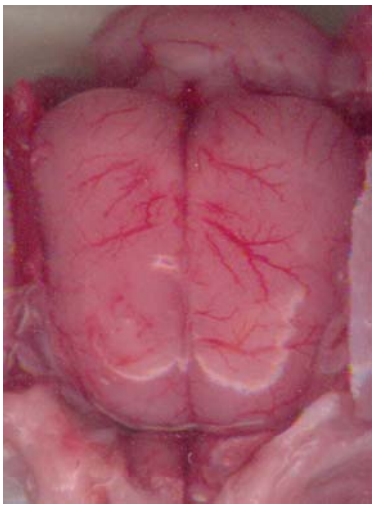

(B)

Fig. 7. Photoacoustic imaging of a rat brain *in situ*. (a) Image of the rat brain cerebral cortex achieved non-invasively with the skin and skull intact. The image size is 2.0 cm×2.0 cm. The vascular structures in the rat cerebral cortex match well with the open-skull anatomical photograph in (B) obtained after the imaging experiment.

3.3 Photoacoustic imaging of rat brain lesions

PAT has been applied to image traumatic lesions in rat brains *in situ*. Laser pulses with a 532-nm wavelength were adopted. The laser beam was expanded and homogenized to provide an incident energy density of <10 mJ/cm^2 on the skin of the rat head, which induced a temperature rise in the skin estimated to be <20 mK. The distribution of optical absorptions in the brain tissues generated proportionate photoacoustic waves which were detected by the 3.5 MHz V383 ultrasonic transducer.

The rat was deeply anesthetized with pentobarbital (100 mg/kg, IP), and the surface of its head was disinfected with alcohol swabs (Isopropyl alcohol 70%). A sterile curved (90° angle) syringe needle (22 G × 1") was inserted through the skin and the skull

bone on the right cortex cerebri to induce a superficial cortical lesion. The rat's brain was imaged immediately by our PAT system with the skin and skull intact. Then, for comparison, an open-skull photograph of the cerebral cortex was taken. The image of the rat brain [see Fig. 8(A)] is compared with the anatomical photograph [see Fig. 8(B)]. The position and the shape of the lesion can be visualized successfully. The absorption contrast between the lesion area and the background parenchyma ranges from 1.7 to 5.2.[17,*]

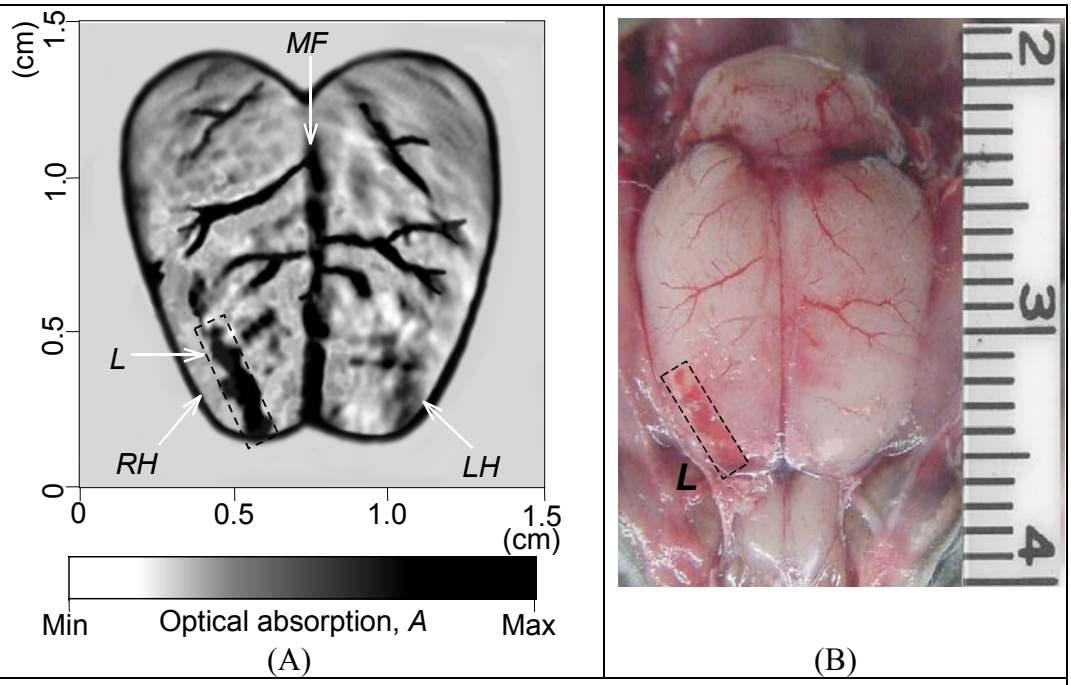

Fig. 8. Photoacoustic imaging of a lesion in a rat brain *in situ*. (A) Non-invasive photoacoustic image of a superficial lesion (1 mm × 4 mm, in the right cortex cerebri—area frontalis) on a rat's cerebra acquired non-invasively with the skin and skull intact. *RH*: right cerebral hemisphere; *LH*: left cerebral hemisphere; and *L*: lesion. The blood vessels distributed on both sides of the median fissure (*MF*) have been imaged clearly. The matrix size of the image is 1,000 (horizontal) × 1,000 (vertical), showing a 1.5 cm × 1.5 cm region. (B) Open-skull photograph of the rat cerebral surface acquired after the imaging experiment.

[*] This material has been published in *Nature Biotechnology* 21 (7), 803–806 (2003). The use of this material has the permission from the corresponding author, Dr. Lihong Wang.

3.4 Photoacoustic imaging of rat brain tumors

Early detection of cancers, followed by proper treatments, can greatly increase the curability. Advances in diagnostic technology will dramatically improve the detection and staging of cancers. However, current detection techniques are mostly geared toward establishing diagnoses of clinically overt cancers. Imaging techniques, such as x-ray computerized tomography (CT), ultrasound, and magnetic resonance imaging (MRI), are limited in their ability to detect small lesions. These techniques leave a narrow window of opportunity for detection before the tumor burden reaches the lethal range. Consequently, there is an imperative need to develop new, non-invasive techniques for early detection of incipient neoplasia.

The hallmarks of cancers include angiogenesis, hyper-metabolism, and invasion into normal adjacent tissues. Optical signals have high sensitivity to these hallmarks and, consequently, can potentially enable early-cancer detection.[46] Due to the hyper-metabolism of cancers, capillaries in cancerous tissues are denser compared to those in normal tissues. Therefore, with higher blood concentrations, the tumor areas have comparatively higher optical absorptions. PAT, with the ability to assess optical absorptions in biological tissues, will potentially contribute to the detection and staging of cancers with satisfactory sensitivity and specificity.

An adult BD-IV rat (~150 g) with developed brain tumors was imaged by this PAT system *in situ*. The rat cell line (Br7-C5) with brain-metastasizing potential and the subsequently derived brain metastatic mammary carcinoma clones were developed in Dr. Stoica's laboratory. The cells when inoculated via the left ventricle (LV-experimental metastasis) consistently metastasized to the brain. The clinical signs (weight loss, lethargy, hunching and ataxia) of brain metastases occurred ~20 days post inoculation.

The skin on the head of the BD-IV rat is black. Therefore, before the imaging experiment, the skin was removed but the skull was left intact. The photoacoustic image of the rat brain cerebral cortex is shown in Fig. 9(A). In this image, three areas have higher optical absorptions compared to the background and have abnormal geometries that are unlikely large blood vessels. These areas in the image are marked with circles. After the imaging experiment, the rat head was opened and vibrotom sections (~200 micrometer per layer) of the rat cerebral cortex were made. On the histology photograph

of a vibrotome section, several brain tumors can be identified [see Fig. 9(B)]. Among them, three tumors with comparatively larger sizes match well with the marked areas in the photoacoustic image. In this experiment, the sizes of the tumors that have been visualized successfully by the PAT system were less than 2 mm.

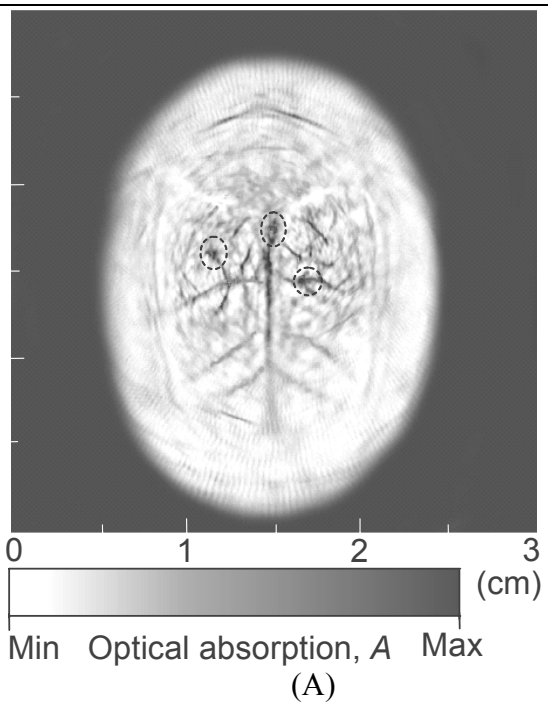

(A)

(B)

Fig. 9. Photoacoustic imaging of rat brain tumors. (A) *In situ* transcranial PAT image of the rat brain cerebral cortex. The marked areas (in circles) in this image have comparatively higher optical absorption and abnormal geometries. (B) Histological photograph of the rat brain cerebral cortex, where several tumors can be identified. Among them, the positions of the three largest tumors (in circles) match well with the photoacoustic image.

3.5 3-D imaging of mouse brains in situ

PAT was applied to non-invasive 3-D imaging of mouse brains *in situ*, where the applied wavelength was 532 nm. Adult BALB/c mice (~50 g, Charles River Breeding Laboratories) were employed in this experiment. The incident energy density of the laser beam was controlled to <10 mJ/cm^2, which induced a temperature rise in the skin estimated to be <20 mK. The 10 MHz XMS-310 ultrasonic transducer was used to detect

the photoacoustic signals. The transducer was driven by a computer-controlled step motor to scan around the mouse head in the horizontal plane (*x*-*y* plane) with a radius of 2.8 cm and a step size of 2°. The transducer and the step motor were fixed on a translation stage to move in the vertical direction, where the scanning range along the *z*-axis was 4.1 cm with a step size of 0.635 mm. The circular scan in the *x*-*y* plane in combination with the linear scan along the *z*-axis constituted a cylindrical scan around the mouse head. The period for each circular scan was 15 minutes, and the total time for 3-D photoacoustic signal acquisition was ~16 hours. Before the experiment, the hair on the mouse head was removed gently using hair remover lotion.

3-D imaging of the mouse brain was achieved non-invasively with the skin and skull intact, as shown in **Error! Reference source not found.**. Images in **Error! Reference source not found.**(A)–(F) show different horizontal cross-sections from the dorsal to the ventral parts of the brain. The color bar indicates the relative optical absorptions in each imaged cross-section, where the red areas—such as the blood vessels—have comparatively higher absorptions. The thickness of the skin and skull covering the mouse brain was ~0.5 mm. The corresponding imaging depths for **Error! Reference source not found.**(A)–(F) increase from 0.5 mm to 8.0 mm with a constant interval of 1.5 mm.

Error! Reference source not found.(A) shows the imaged cross-section corresponding to the cortical surface of the mouse brain, where the vascular distribution in the superficial cortex can be visualized clearly. Images in **Error! Reference source not found.**(B)–(F) present the interior brain structures underneath the superficial cortex. For illustration, images in **Error! Reference source not found.**(D) and (F) are compared with their corresponding histological pictures in **Error! Reference source not found.**(G) and (H), respectively.[47] A satisfactory match between them can be seen, which demonstrates that the characteristic tissue structures in the mouse brain can be visualized clearly and accurately through the skin and skull employing this PAT system. Because the absorption coefficient of the blood (>100 cm^{-1} at 532-nm wavelength) is much larger than the absorption coefficient of the gray and white matters of the brain (~0.56 cm^{-1} at 532-nm wavelength)[48,49], the major photoacoustic signals are provided by the optical

absorption of blood. Therefore, the contrast presented by these photoacoustic images actually reveals the blood hemoglobin concentrations in various brain tissues.[19,*]

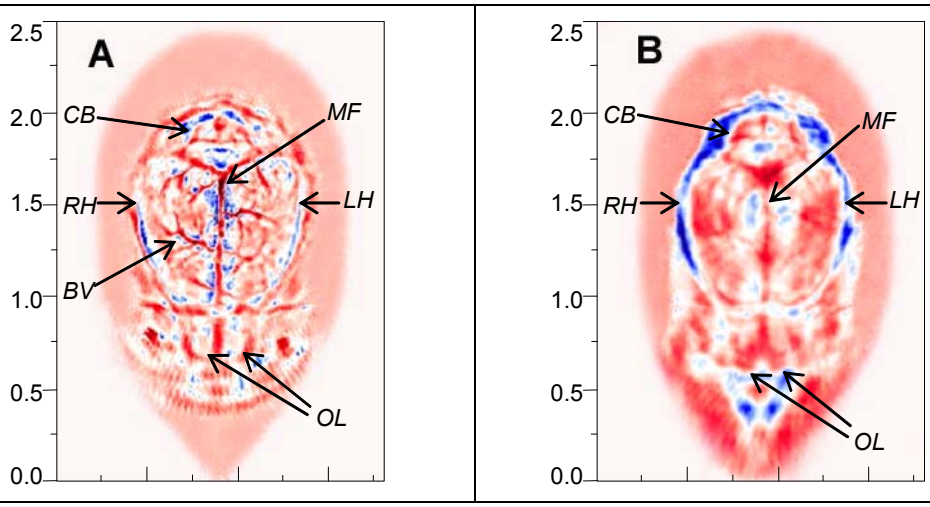

Fig. 10. 3-D photoacoustic imaging of a mouse brain. The imaging of the mouse brain has been achieved non-invasively with the skin and skull intact. The images in (A)–(F) show horizontal cross-sections from the dorsal to the ventral parts of the brain, where the imaging depths are 0.5 mm, 2.0 mm, 3.5 mm, 5.0 mm, 6.5 mm and 8.0 mm, respectively, from the top surface of the mouse head. The size of each image is 1.8 cm×2.5 cm. A color bar shows the magnitude of relative optical absorptions, where the red areas indicate tissues with comparatively higher optical absorptions. Histological pictures in (G) and (H) are presented for comparison with the corresponding images in (D) and (F), respectively. In photoacoustic images and histological pictures, the major characteristic tissue structures in the mouse brain are indicated. *BV*: blood vessel; *CB*: cerebellum; *FLC*: fissura longitudinalis cerebri; *FTC*: fissura transversa cerebri; *HC*: hippocampus; *LH*: left hemisphere; *MC*: mesencephalon; *MF*: median fissure; *OL*: olfactory lobes; *RH*: right hemisphere; and *VL*: ventriculi lateralis.

[*] This material has been published in *Optics Letters* 28, 1739–1741 (2003).

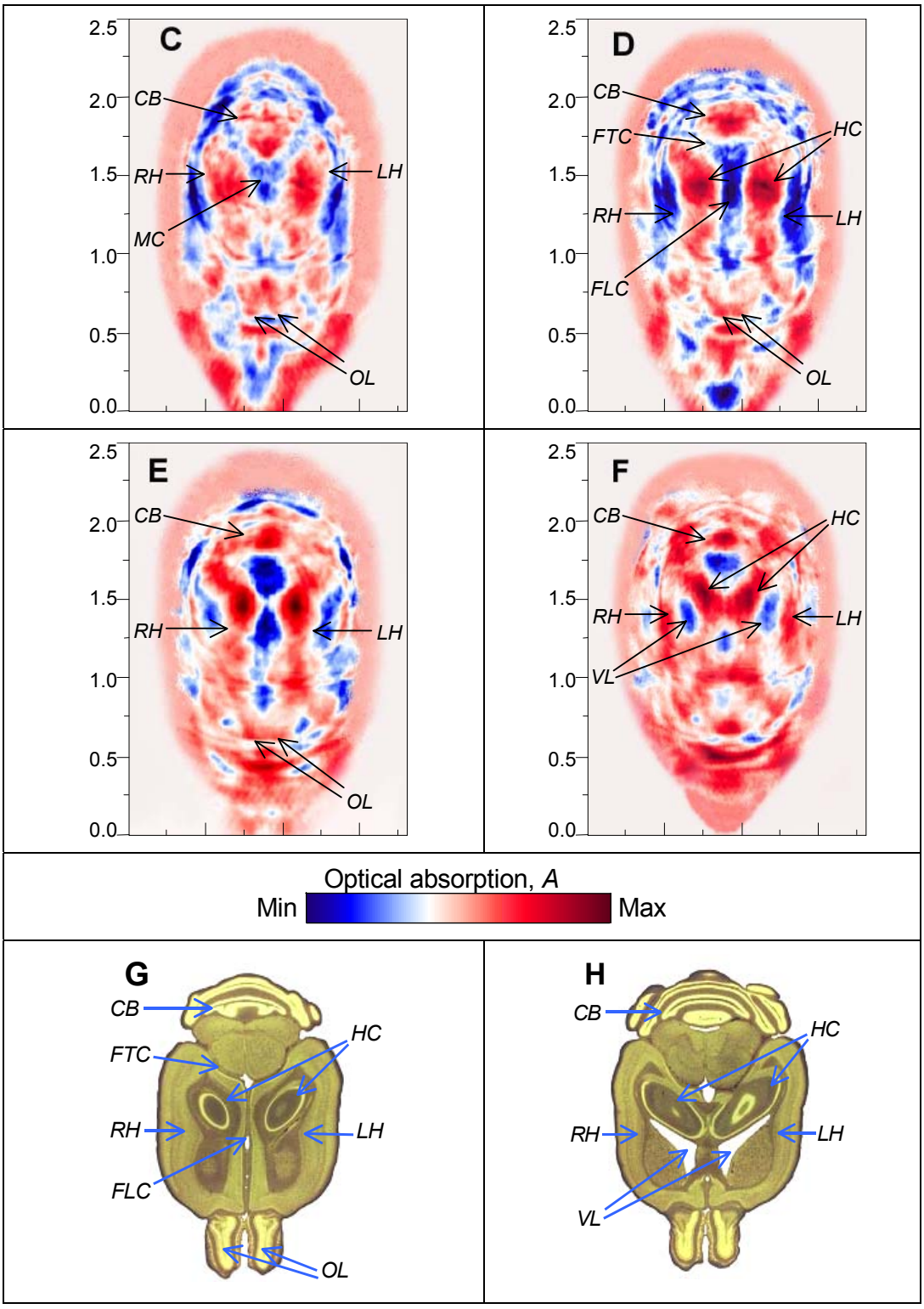

Figure 10 continued.

3.6 Spatial resolution

Employing the full-view circular-scan geometry and the modified back-projection algorithm, point-by-point distribution of optical absorption in a biological sample can be accurately reconstructed from the detected photoacoustic signals. The spatial resolution of this PAT system is primarily diffraction-limited by the detected photoacoustic signals. Through the analysis of photoacoustic signals from animal brains detected by the 10 MHz XMS-310 transducer, the cutoff frequency f_c is ~20 MHz; while with the 3.5 MHz V383 transducer, the cutoff frequency f_c is ~6 MHz. The FWHM of the point spread function (PSF) for this imaging system is estimated as $0.8c_s / f_c$,[50] where the acoustic velocity c_s in biological tissues is ~1.5 km/s. Accordingly, the highest achievable spatial resolution of this imaging system on small-animal brains is ~60 μm with the 10 MHz XMS-310 transducer (or ~200 μm with the 3.5 MHz V383 transducer), which matches our experimental results on phantom samples.[51]

4. Functional PAT of Small-animal Brains *in vivo*

Functional imaging of small animals, such as rats and mice, is a vital tool in the study of diseases. Non-invasive, quantitative and repetitive imaging of biological processes in living animals changes the way in which many experiments in models of human diseases and normal physiological processes are conducted. Animal models of human diseases, such as cancers and Parkinson's disease, are providing us knowledge about the causes, diagnosis and therapy of these diseases, and are offering us the opportunity to evaluate pathologic progressions in much-compressed time frames.

Because brain is highly responsive to changes in blood oxygenation and blood flow, high-speed and high-resolution mapping of the concentration of total hemoglobin (HbT) and the hemoglobin oxygen saturation (SO_2) is of great significance in neurophysiology, neuropathology and neurotherapy. For example, visualizing functional parameters of brain cancers and traumatic brain injuries, monitoring ischemia and shock, and studying neuronal activities are of interest. Despite decades of efforts, however, no technique has been developed up to now that is clinically feasible for high-resolution, accurate, continuous and non-invasive imaging of HbT and SO_2 in organs, such as brain.

Novel functional imaging techniques, in addition to functional MRI and positron emission tomography (PET), will advance neuroscience significantly.

Optical measurement of brain is highly desirable because it is functional[33-36]. Brain physiology and pathology are associated with optical properties including absorption, scattering and fluorescence of brain tissues, which is well known and widely employed in medicine.[33] Based on optical contrast, optical imaging modalities, such as near-infrared spectroscopy (NIRS), can visualize dynamic and functional properties of neurosystems, such as cerebral blood volume and cerebral blood oxygenation.[4,33] Its advantage over MRI is that optical contrast can assess simultaneously both oxy- and deoxy-hemoglobin[52, 53] and can also detect intracellular events related to neuronal activities with a fast and direct response to stimulation.[54] Pure-optical modalities for neuroimaging, however, have significant drawbacks due to the overwhelming scattering of optical waves in biological tissues. For example, NIRS has so far been proved incapable of providing satisfactory resolution and accuracy for imaging of brain through the intact skull. Invasive open-skull imaging has no depth resolution and is only limited to brain surface.[55–57]

The functional photoacoustic technique was applied for the first time on small-animal brains. With its non-invasive characteristic, this technique enables continuous monitoring on a single animal sample and hence can reduce the number of animals required and the time needed to conduct a study. With the advantage of high-resolution, this technique can achieve satisfactory imaging quality on small animals. Based on the intrinsic contrast of optical absorptions in brain tissues, functional PAT can visualize dynamic and functional activities in the brain. Functional PAT has been employed to visualize 1) rat cerebral hemodynamic responses to neuronal activities induced by whisker stimulations, and 2) changes in rat cerebral hemoglobin concentration and oxygenation induced by systemic physiological modulations, including hyperoxia, normoxia and hypoxia.

4.1 PAT of rat brains in vivo

The brains of adult Sprague Dawley (SD) rats (~120 g, Charles River Breeding Laboratories) were employed in this experiment. Before imaging, the hair on each rat's

head was removed using hair remover lotion. A dose of 87 mg/kg Ketamine plus Xylasine 13 mg/kg administered intramuscularly was used to briefly anesthetize the rat and supplemental injections of a similar anesthetic mixture (~10 mg/kg/hour) kept the rat motionless throughout the experiment. The rat head was fixed steadily by a homemade animal holder through two ear pins and a breathing mask that also provided the rat with breathing gas. The animal holder effectively kept the rat head motionless during the acquisition of photoacoustic signals. The average thicknesses of the skin and the skull covering the brain were ~0.8 and 0.6 mm, respectively. Laser light penetrated to the rat brain through the skin and the skull which homogenized the incoming light further by scattering. After the data acquisition for PAT, the rat was sacrificed using pentobarbital (120 mg/kg, IP). Subsequently, an open-skull photograph of the brain surface was taken as a control. The 10 MHz XMS-310 transducer was employed to acquire the photoacoustic signals. In this experiment, light pulses at 584 nm and 600 nm were applied respectively. At these two wavelengths, the incident energy densities were similar. For each pulse, the energy density was ~3 mJ/cm^2 on the surface of the rat head, which induced a temperature rise in the brain vessels estimated to be <15 mK.

Photoacoustic images corresponding to the 584-nm and 600-nm wavelengths are shown in Fig. 11(A) and (B), respectively. Based on the absorption contrast between blood and background brain tissues, both of them present the vasculature in the rat brain cerebral cortex successfully and match well with the open-skull anatomical photograph obtained after the imaging experiment [see Fig. 11(C)]. In the brain images, the optical absorption is shown by a gray scale, where the brighter areas have higher absorptions.

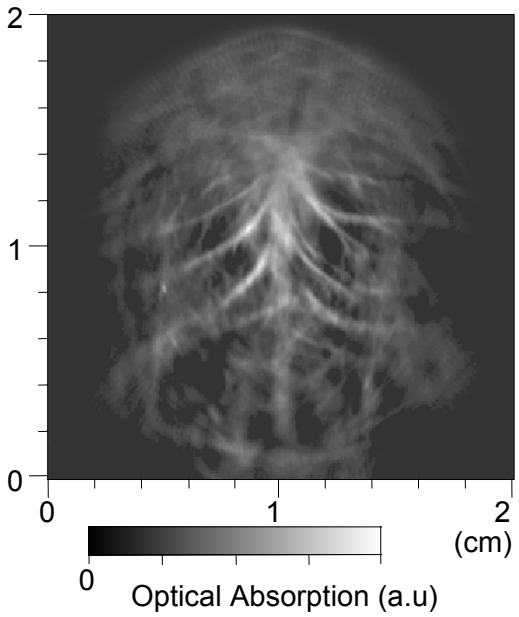

(A)

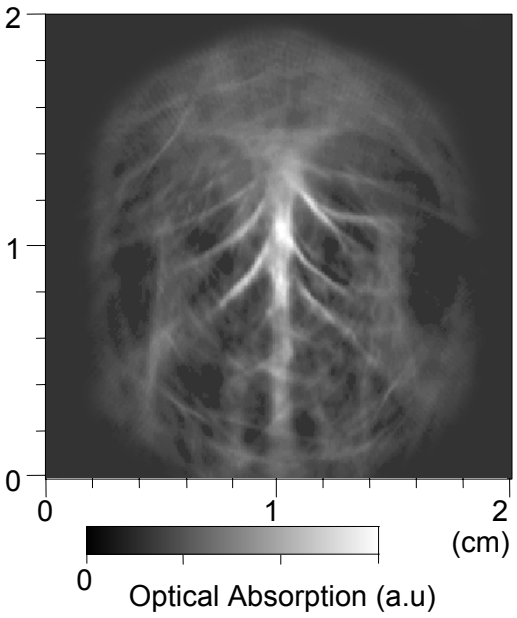

(B)

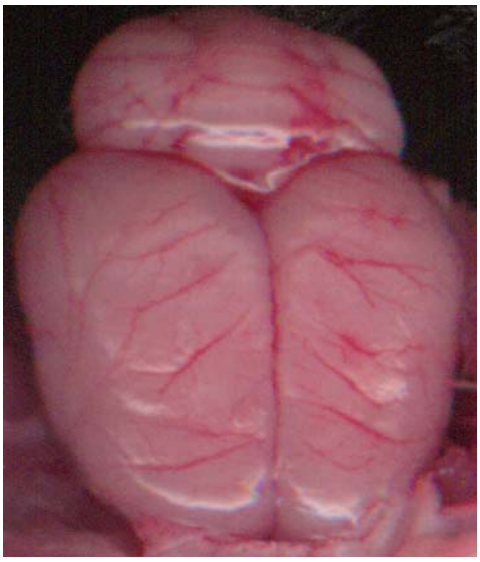

(C)

Fig. 11. Non-invasive photoacoustic imaging of a rat brain *in vivo*. Images of the vascular structure in the rat brain cerebral cortex generated by (A) 584-nm and (B) 600-nm laser light, respectively. (C) Open-skull anatomical photograph obtained after the imaging experiment.

4.2 PAT of cerebral hemodynamics in response to neuronal activities

Our PAT system was employed to visualize the functional representations of whiskers in the cerebral cortex of rats. While stimulating the left-side and the right-side whiskers, respectively, we obtained two corresponding photoacoustic images of a rat's superficial cortex. Subtracting the photoacoustic image without whisker stimulations from the two photoacoustic images with whisker stimulations produced two maps of functions evoked by the corresponding whisker stimulations.

Functional cerebral hemodynamic changes in response to whisker stimulations on either side of the rat snout were successfully imaged [see Fig. 12(B) and (C)]. The imaged distributions of functional signals match the vascular patterns in the activated regions well [Fig. 12(A)], which indicates that in this experiment the functional signals detected by PAT came from hemodynamic changes in the large blood vessels in the superficial cortex. The activated regions visualized by PAT are marked on the photograph of the brain cortical surface by two dotted frames [see Fig. 12(D)]. Since the activated region lies in the hemisphere corresponding to the opposite side whisker stimulations, the observed changes in photoacoustic signals are believed to be induced by the whisker activities. After the imaging, the rat recovered normally without noticeable health problems. After the rat had been scarified, a histochemistry processing was performed of its cerebral cortex. The vibrotome sections of cortical layer IV of the specialized region of the rat cerebral cortex—termed the whisker-barrel cortex [see Fig. 12(E)]—co-localize well with the activated regions in the functional images.

It is widely accepted that increases in neuronal activity are accompanied by increases in local cerebral blood flow and regional metabolic activity in the homonymous activated region.[58,59] The PAT system enables us, by non-invasive means, to localize the hemodynamic responses clearly and accurately to neuronal activities and metabolic increases as a consequence of whisker stimulations. The detected differential optical absorption results from a complex interplay of blood volume, flow, and oxygen consumption. Because deoxy- and oxy-hemoglobin have similar extinction coefficients at 532-nm wavelength, the dominant factor that intensified the photoacoustic signals in this experiment is believed to be an increase in vascular blood volume (or flow) in the activated region around the whisker-barrel cortex during the stimulation. The observed

fractional change in optical absorption, $\Delta A / A$, in the large blood vessels within the activated regions was up to 8%. The functional photoacoustic images are characterized by a strong vascular pattern, which is believed to result from an increased inflow of fresh blood. The areas of vascular response are clearly wider than the whisker-barrel cortex regions, as hemodynamic changes propagate through the feeding vessels and even spread to neighboring vessels.[*,17]

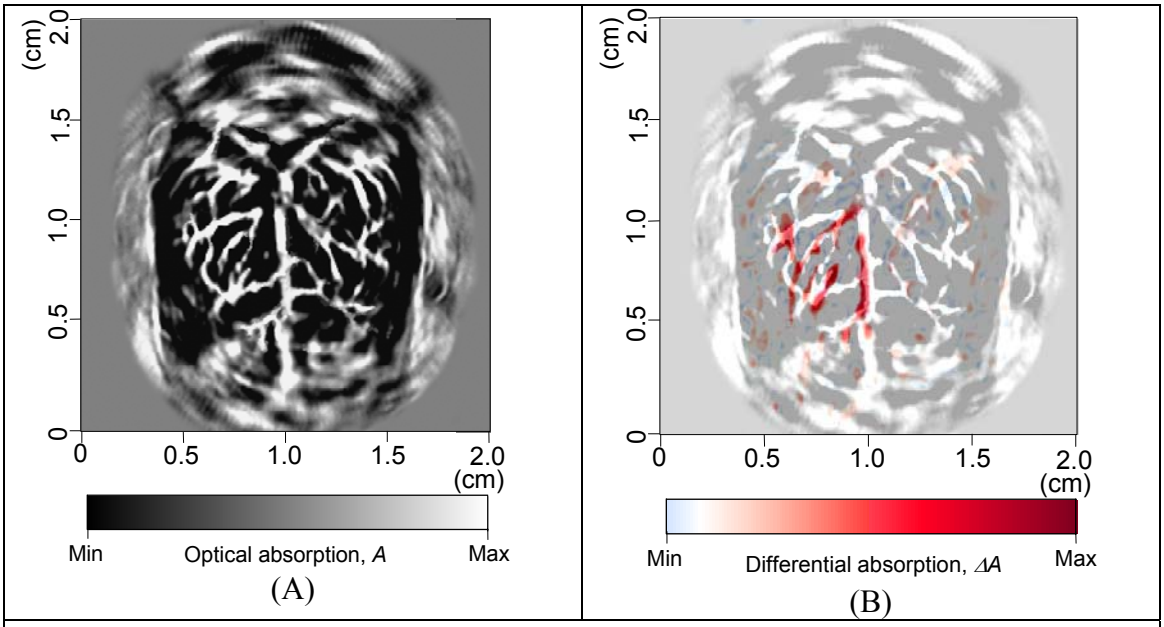

Fig. 12. Non-invasive functional imaging of cerebral hemodynamics. The functional changes in a rat brain cerebral cortex were induced by whisker stimulations. (A), Photoacoustic image of the vascular pattern in the rat superficial cortex. (B) and (C), Non-invasive functional images corresponding to the left-side and the right-side whisker stimulations, respectively, acquired non-invasively with the skin and skull intact. These two maps of functional representations of whiskers are superimposed on the image of the vascular pattern in the superficial cortex shown in (A). (D), Open-skull photograph of the rat cerebral cortex obtained after the imaging experiment. *B*: bregma; *L*: lambda; *M*: midline; *A*: activated regions corresponding to whisker stimulations (4 mm × 4 mm). (E), Histology of normal lamina IV cortical barrels, located in regions *A*, representing the large mystacial vibrissae of the rat somatosensory system (40X Mag.)

[*] This material has been published in *Nature Biotechnology* 21 (7), 803–806 (2003). The use of this material has the permission from the corresponding author, Dr. Lihong Wang.

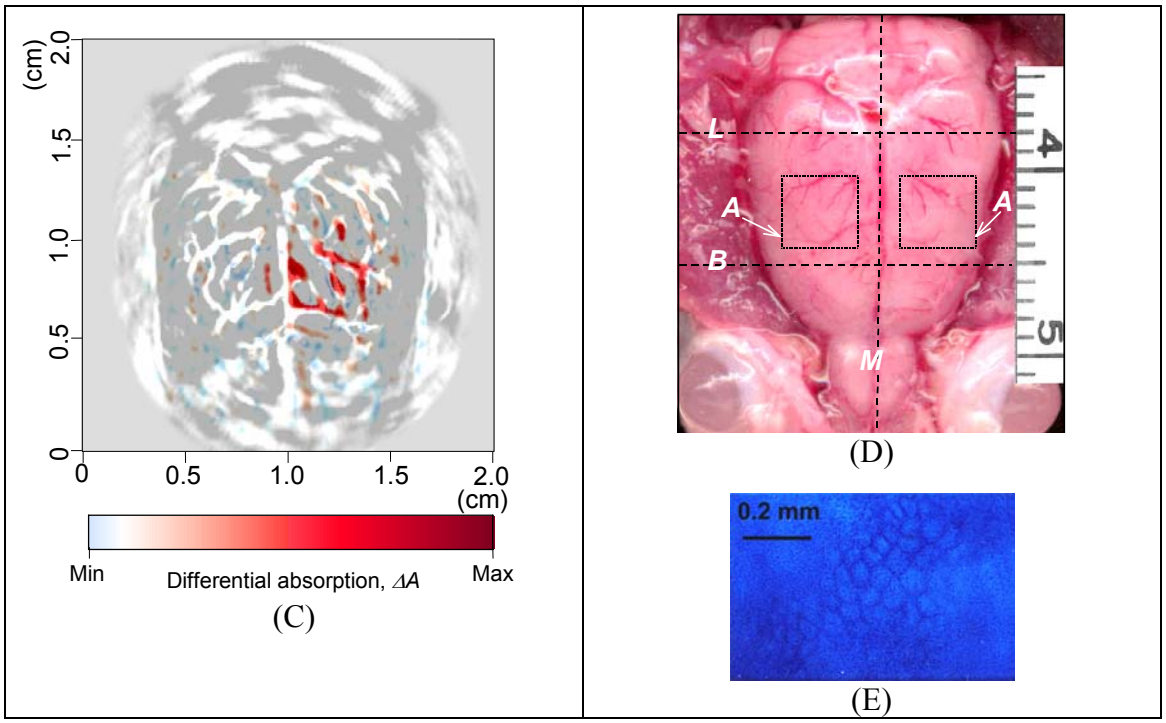

Figure 12 continued.

4.3 Spectroscopic PAT of hemoglobin concentration and oxygenation

4.3.1 Introduction

After we achieved non-invasive photoacoustic imaging of small-animal brains *in vivo* based on intrinsic optical contrast, PAT employing multiple wavelengths was explored to study the functional parameters, including cerebral blood volume and blood oxygenation, in small-animal brains. Similar to NIRS, functional PAT of blood SO_2 and HbT relies on the spectroscopic differences between oxygenated hemoglobin (HbO_2) and deoxygenated hemoglobin (Hb). Assuming that HbO_2 and Hb are dominant absorption compounds in a biological sample in the spectral region under study, photoacoustic measurements of the sample at two wavelengths respectively are sufficient for an absolute estimation of blood oxygenation and a relative estimation of blood volume. In contrast to NIRS that measures diffuse light transmission, PAT detects the weakly scattered photoacoustic signals (ultrasonic waves) that are produced directly by optical absorption. Even complex biological structures, such as brain vasculature, can be imaged by PAT with satisfactory spatial resolution, which is primarily limited by the bandwidth of detected photoacoustic signals. The ability to image hemoglobin concentration and oxygenation simultaneously with high spatial resolution will permit detailed quantitative analysis of the spatiotemporal hemodynamics of functional brain activities, including imaging of oxygen metabolism.

4.3.2 Multi-wavelength functional PAT system

The tunable dye laser pumped by the Nd:YAG laser provided laser irradiation pulses. The incident energy density of the laser beam was controlled to <3 mJ/cm^2 on the surface of the rat head, which, attenuated and homogenized further by the skin and skull, induced a temperature rise in the brain vessels estimated to be <15 mK. The 10 MHz XMS-310 ultrasonic transducer was employed in this experiment for signal acquisition. The non-focused transducer can realize high-quality two-dimensional imaging of the rat brain cortex through a circular scan because large venous vessels are distributed in the

cortical surface that provide dominant photoacoustic signals. The signals from the blood vessels in the ventral brain are relatively small due to the attenuation of light in the brain.

4.3.3 Spectroscopic imaging of HbT and SO_2

In optical measurements of hemoglobin concentration and oxygenation, assuming that Hb and HbO_2 are dominant absorbing compounds at the applied two wavelengths λ_1 and λ_1, HbT and SO_2 can be calculated with the detected optical absorptions at the two wavelengths:[33,60,61]

$$\mathrm{HbT} = [\mathrm{HbO_2}] + [\mathrm{Hb}] = \frac{\mu_a^{\lambda_1}\varepsilon_{\Delta\mathrm{Hb}}^{\lambda_2} - \mu_a^{\lambda_2}\varepsilon_{\Delta\mathrm{Hb}}^{\lambda_1}}{\varepsilon_{\mathrm{Hb}}^{\lambda_1}\varepsilon_{\mathrm{HbO_2}}^{\lambda_2} - \varepsilon_{\mathrm{Hb}}^{\lambda_2}\varepsilon_{\mathrm{HbO_2}}^{\lambda_1}}, \tag{5}$$

$$\mathrm{SO_2} = \frac{[\mathrm{HbO_2}]}{[\mathrm{HbO_2}] + [\mathrm{Hb}]} = \frac{\mu_a^{\lambda_2}\varepsilon_{\mathrm{Hb}}^{\lambda_1} - \mu_a^{\lambda_1}\varepsilon_{\mathrm{Hb}}^{\lambda_2}}{\mu_a^{\lambda_1}\varepsilon_{\Delta\mathrm{Hb}}^{\lambda_2} - \mu_a^{\lambda_2}\varepsilon_{\Delta\mathrm{Hb}}^{\lambda_1}}, \tag{6}$$

where μ_a ($\mathrm{cm^{-1}}$) is the absorption coefficient; $\varepsilon_{\mathrm{Hb}}$ and $\varepsilon_{\mathrm{HbO2}}$ are the known molar extinction coefficients ($\mathrm{cm^{-1}\ M^{-1}}$) of Hb and HbO_2, respectively; $\varepsilon_{\Delta\mathrm{Hb}} = \varepsilon_{\mathrm{HbO_2}} - \varepsilon_{\mathrm{Hb}}$; and $[\mathrm{Hb}]$ and $[\mathrm{HbO_2}]$ are the concentrations (M) of the two forms of hemoglobin, respectively.

By irradiating a rat head with light of two wavelengths, λ_1 and λ_1, independently, one can get two photoacoustic images. These two images, after normalized by considering the incident light energy densities and the attenuations of light energy by the skin and skull, represent the distributions of relative optical absorptions $A^{\lambda_1}(\mathbf{r})$ and $A^{\lambda_2}(\mathbf{r})$ in the cerebral cortex corresponding to the two wavelengths. By substituting $\mu_a^{\lambda_1}$ and $\mu_a^{\lambda_2}$ in Eqs. (5) and (6) with $A^{\lambda_1}(\mathbf{r})$ and $A^{\lambda_2}(\mathbf{r})$, one can calculate point-by-point images of an absolute estimation of SO_2 and a relative estimation of HbT.

The spectral region applied in this work was between 580 nm and 600 nm. In this region, the absorption contrast between blood and background brain tissues was high enough to provide satisfactory imaging quality. Meanwhile, the penetration depth of light in this region even in blood was similar to or greater than the size of the imaged brain vessel branches (<50 μm). Moreover, Hb and HbO_2 were the only chormophores of

significance, and scattering was assumed to be constant over this region. The relative extinction coefficients of Hb and HbO_2 in the applied spectral region were detected by photoacoustic measurements of rat blood samples with known SO_2 levels and then were used in the calculations of HbT and SO_2 in the *in vitro* and *in vivo* experiments.

4.3.4 Test on phantom samples

The sensitivity and accuracy of this multi-wavelength spectroscopic PAT system to HbT and SO_2 were tested with phantom samples of mixed dye solutions. Two dyes, Fiesta Red and Lake Placid Blue (PenCity, GA) were employed to mimic HbO_2 and Hb, respectively. The absorption coefficients of these two dyes at 580-nm and 600-nm wavelengths were measured. These two dyes were mixed according to different ratios and diluted to various concentrations. Each mixed dye solution was injected into a soft and transparent tube with an inner diameter of 0.2 mm and then irradiated by laser pulses at 580 nm and 600 nm, respectively. Intensities of photoacoustic signals from each mixed dye solution were used to calculate two parameters: 1) the total dye concentration, [Red]+[Blue]; and 2) the fraction of the red dye concentration in the total dye concentration, [Red]/([Red]+[Blue]).

In the experiment for testing the sensitivity of this PAT system to HbT, first we made three mother liquids of mixed dyes, where the ratios between [Red] and [Blue] were 3:1, 1:1, and 1:3 respectively. Then each mother liquid was diluted with water to achieve 10 different concentrations evenly distributed from 10% to 100%. In the three charts in Fig. 13, where the results corresponding to the three mother liquids are presented respectively, the *y*-axes show the measured total dye concentrations, [Red]+[Blue], that match well the preset concentrations on the *x*-axes. The ratio between [Red] and [Blue] shows no effect on the measurement of the total dye concentration.

In another experiment for testing the sensitivity of this PAT system to SO_2, dye solutions with different ratios between [Red] and [Blue] were measured, where the fraction of [Red]/([Red]+[Blue]) changed from 0% to 100% with a constant interval of 10%. The measurements in Fig. 14 match well with the preset fraction of [Red]/([Red]+[Blue]). The experimental results on the phantom samples proved the

capability of this PAT system to discriminate absorbing materials mixed together based on their distinct absorption spectra.

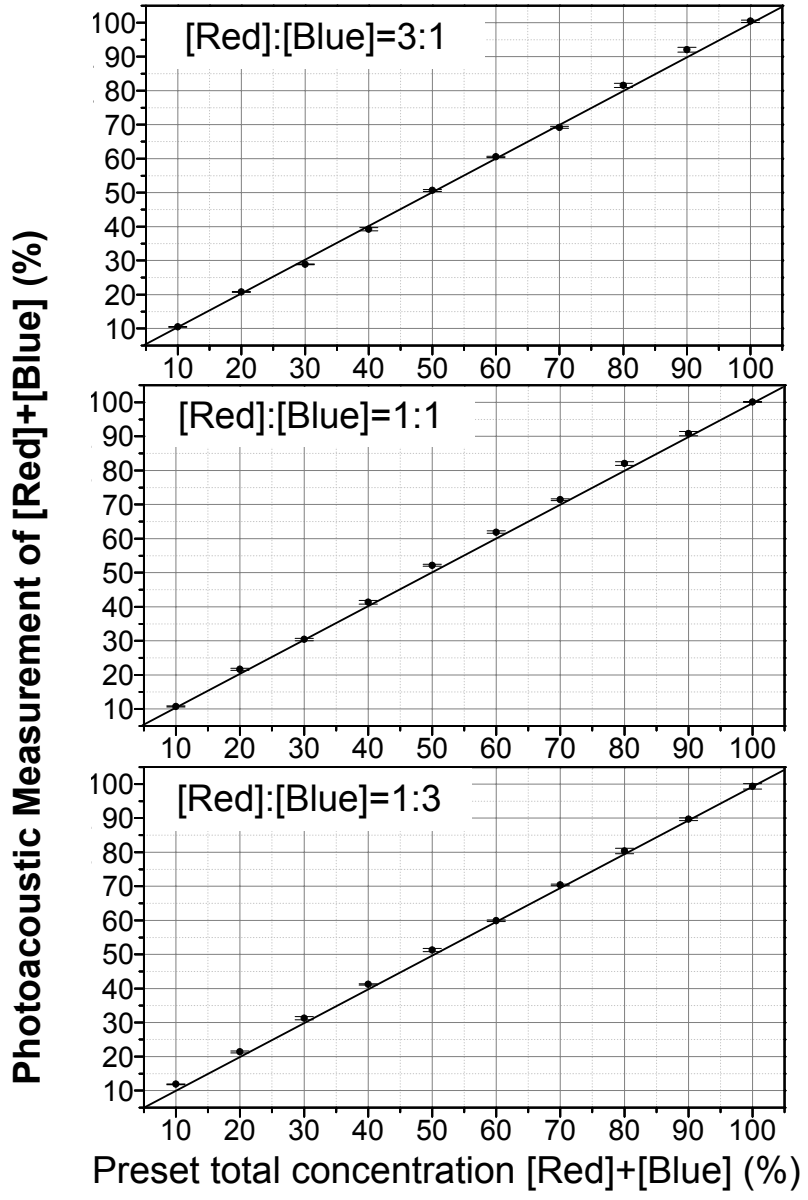

Fig. 13. Spectroscopic measurement on phantom samples (HbT). Photoacoustic measurement of the total dye concentration, [Red]+[Blue], in each mixed dye solution containing Fiesta Red and Lake Placid Blue, where the ratios between [Red] and [Blue] are 3:1, 1:1 and 1:3 respectively for the three charts.

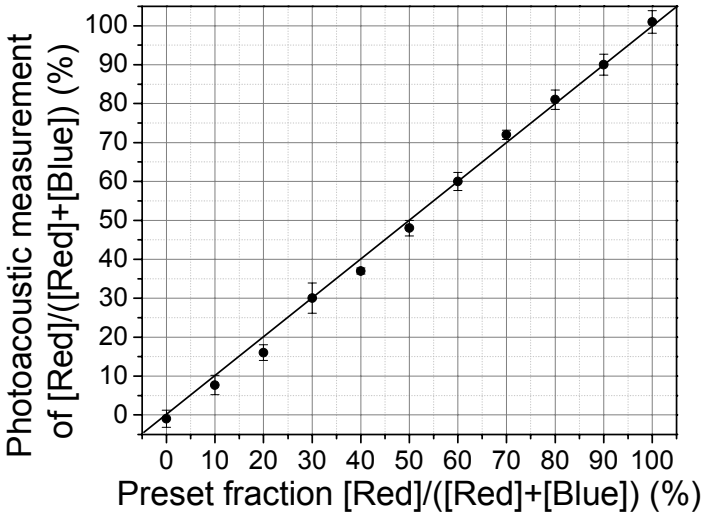

Fig. 14. Spectroscopic measurement on phantom samples (SO_2). Photoacoustic measurement of the fraction of the red dye concentration in the total dye concentration, [Red]/([Red]+[Blue]), in each mixed dye solution.

4.3.5 Photoacoustic measurement of rat blood SO_2 *in vitro*

This spectroscopic PAT system has been applied to measure the SO_2 levels of rat blood samples *in vitro*. A blood sample with a high SO_2 level was collected from a rat ventilated with pure oxygen and another blood sample with a low SO_2 level was collected from a rat whose breath was hold. Each sample was diluted respectively 1:5 with PBS buffer containing anticoagulant. These two diluted blood samples were mixed with different ratios to achieve various SO2 levels from 64.1% to 95.0% measured by a Co-Oximeter (Irma 2000 SL, Diametrics). Then each mixed blood sample was injected into a 0.2 mm inner-diameter transparent tube and measured by the PAT system at two wavelengths, 580 nm and 595 nm, respectively. With the detected intensities of the photoacoustic signals at the two wavelengths, the SO_2 level of every mixed blood sample was calculated, which, after an alignment, matched well with the standard value provided by the Co-Oximeter (see Fig. 15).

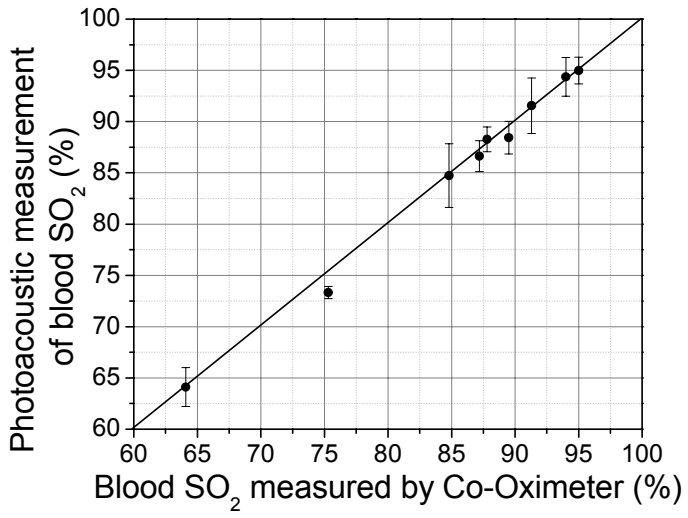

Fig. 15. Photoacoustic measurements of blood SO_2 *in vitro*. The oxygen saturation of hemoglobin (SO_2) in rat blood samples were measured and compared with the standards provided by the Co-Oximeter.

4.3.6 Animal protocol

We performed functional photoacoustic imaging of rat brains *in vivo* to demonstrate the capability of this technique to assess simultaneously cerebral blood volume and oxygenation. Sprague Dawley rats (~80 g, Charles River Breeding Laboratories) were used in this study. All experimental animal procedures were carried out in conformity with the guidelines of the United States National Institutes of Health (Guide for the Care and Use of Laboratory Animals, NIH Publication No. 86-23, revised 1985. US Government Printing Office, Washington DC). The laboratory animal protocol for this work was approved by the ULAC of Texas A&M University.

Before imaging, the hair on the rat head was removed using hair remover lotion. A dose of 87 mg/kg Ketamine plus Xylasine 13 mg/kg, administered intramuscularly, was used to anesthetize the rat and supplemental injections of a similar anesthetic mixture (~50 mg/kg/hour) kept the rat motionless throughout the experiment. Through a breathing mask, inhaled gas was ventilated to the rat at a flow rate of ~0.6 l/min. The oxygen concentration in the inhaled gas was adjustable through a gas proportioner meter (GMR2, Aalborg). During the *in vivo* experiment, the sensor of a Pulse-Oximeter (8600 V, Nonin

Medical, Inc.) clamped a hind foot of the rat to monitor the global arterial blood oxygenation. Through the modulation of the inhaled oxygen concentration, the rat experienced three systemic physiological statuses, hyperoxia, normoxia and hypoxia. Under each status, laser light at 584 nm and 600 nm were applied respectively to generate photoacoustic images of the cerebral cortex. The *in vitro* measurements on the skin and skull of another rat from the same group indicated that at the 584-nm wavelength, ~10% light energy can penetrate through the skin and skull; while at the 600-nm wavelength, ~15% light energy can penetrate through the skin and skull.

The *in vivo* experiment was performed according to the following steps. Firstly, the rat was provided with pure oxygen and its global arterial blood oxygenation was ~99% according to the Pulse-Oximeter. Under the hyperoxia condition, two images corresponding to the two wavelengths were acquired. Then, the inhaled gas was altered slowly from pure oxygen to normal air. The status of the rat changed from the hyperoxia to the normoxia and the arterial blood oxygenation dropped to ~93%. Under the normoxia status, we also acquired two images corresponding to the same two wavelengths. In the following, the inhaled gas was altered slowly to hypoxic gas (~8% O_2, ~5% CO_2 and ~87% N_2) and consequently the arterial blood oxygenation of the rat dropped to ~80%. Under the hypoxia status, another two images were acquired. Hence, totally, we acquired six images corresponding to the three statuses at the two wavelengths. After the data acquisition for imaging, the rat recovered normally without noticeable health problems. Finally, the rat was sacrificed using pentobarbital (120 mg/kg, IP). The skin and skull of the rat were removed and an open-skull photograph of the brain cortex was taken as a control.

4.3.7 *In vivo* experimental results

Fig. 16(A)-(F) are the images of relative optical absorptions $A^{\lambda}(\mathbf{r})$ in the rat brain cerebral cortex corresponding to the three physiological statuses at the 584-nm and 600-nm wavelengths, respectively. With the high optical absorption contrast between blood and background brain tissues, all the brain images show the vascular branches in the cerebral cortex clearly and match well with the open-skull anatomical photograph

obtained after the imaging experiment [see Fig. 16(Q)]. Before the calculations for HbT and SO_2, the areas of imaged vascular branches that were all cortical venous vessels were segmented from the background. The threshold was the averaged intensity of relative optical absorption in the imaged brain area. Then, with Eqs. (5) and (6), we calculated the point-by-point distributions of HbT and SO_2 in the areas of large vessels under the three physiological statuses [see Fig. 16(G)-(L)], where the color bars for the SO_2 images indicate the absolute values while the color bars for the HbT images have an arbitrary unit. The averaged SO_2 levels in the imaged venous vessels were ~80%, ~70% and ~57% under the hyperoxia, normoxia and hypoxia statuses, respectively.

Based on the spectroscopic PAT, the functional changes of SO_2 and HbT in the rat cerebral cortex as results of the physiological modulations can be analyzed quantitatively or semi-quantitatively. Under the hyperoxia status, the averaged SO_2 level in the areas of imaged cortical venous vessels in the rat brain was ~10% higher than that under the normoxia status; while under the hypoxia status, the averaged SO_2 level was ~13% lower than that under the normoxia status [see Fig. 16(M) and (N)]. Simultaneously, the averaged HbT in the areas of imaged cortical venous vessels presented a relative increase of ~12% as a result of the change from the normoxia to the hypoxia, which was comparatively larger than the ~4% relative difference in HbT between the hyperoxia status and the normoxia status [see Fig. 16(O) and (P)]. The functional images in Fig. 16(M)-(P) are superimposed on the structural image of the cortical vasculature shown in Fig. 16(B). The functional changes observed in this experiment matched the well-established model about the effects of hyperoxia and hypoxia on the physiological parameters in the brain.[62,63]

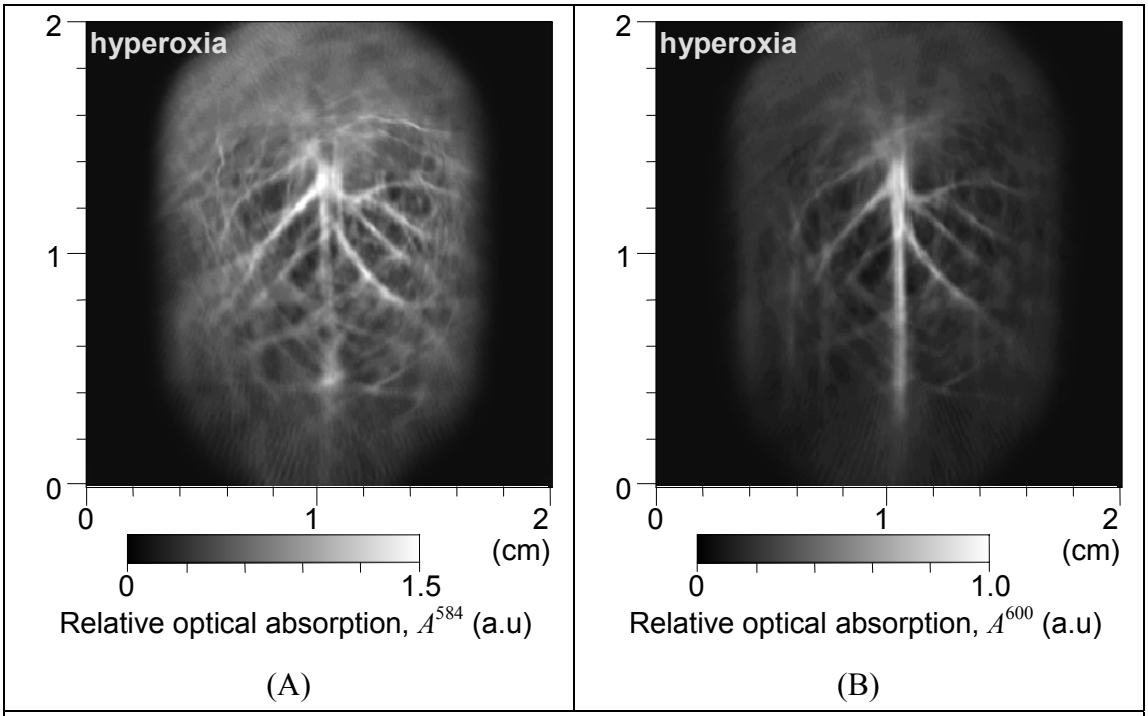

Fig. 16. Non-invasive photoacoustic imaging of cerebral HbT and SO_2. The functional parameters, total concentration of hemoglobin (HbT) and the hemoglobin oxygen saturation (SO_2), in the cerebral cortex of a rat brain were altered by systemic physiological modulations including hyperoxia, normoxia and hypoxia. (A) and (B), Brain images generated by 584-nm and 600-nm laser light respectively under the hyperoxia status. (C) and (D), Brain images generated by 584-nm and 600-nm laser light respectively under the normoxia status. (E) and (F), Brain images generated by 584-nm and 600-nm laser light respectively under the hypoxia status. (G) and (H), Images of SO_2 and HbT in the areas of cortical venous vessels under the hyperoxia status. (I) and (J), Images of SO_2 and HbT in the areas of cortical venous vessels under the normoxia status. (K) and (L), Images of SO_2 and HbT in the areas of cortical venous vessels under the hypoxia status. (M), Averaged differential image of SO_2 in the cortical venous vessels between the hyperoxia status and the normoxia status; hyperoxia–normoxia. (N), Averaged differential image of SO_2 in the cortical venous vessels between the hypoxia status and the normoxia status; hypoxia–normoxia. (O), Averaged differential image of HbT in the cortical venous vessels between the hyperoxia status and the normoxia status; (hyperoxia–normoxia)/normoxia. (P), Averaged differential image of HbT in the cortical venous vessels between the hypoxia status and the normoxia status; (hypoxia–normoxia)/normoxia. (Q), Open-skull anatomical photograph of the brain.

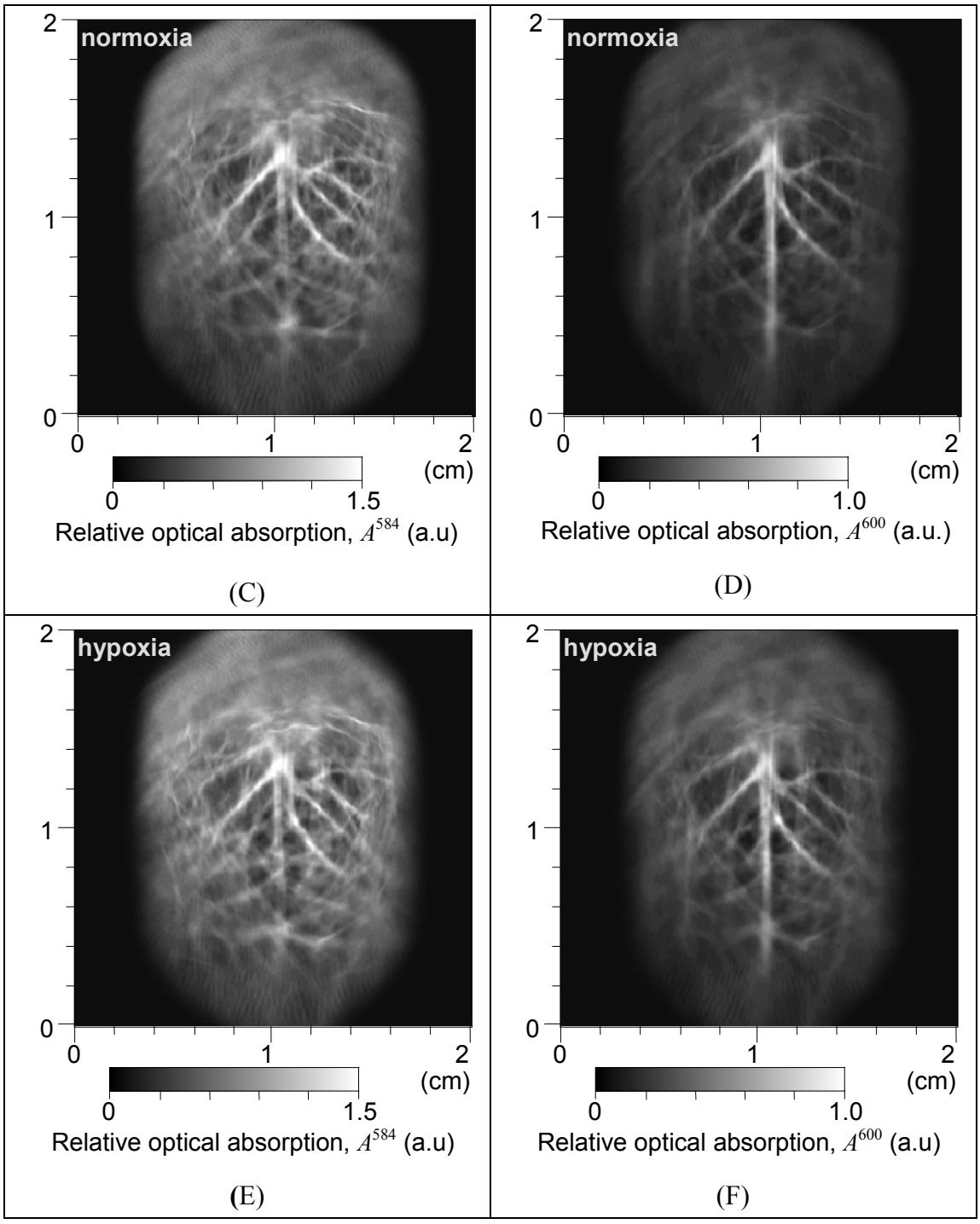

Figure 16 continued.

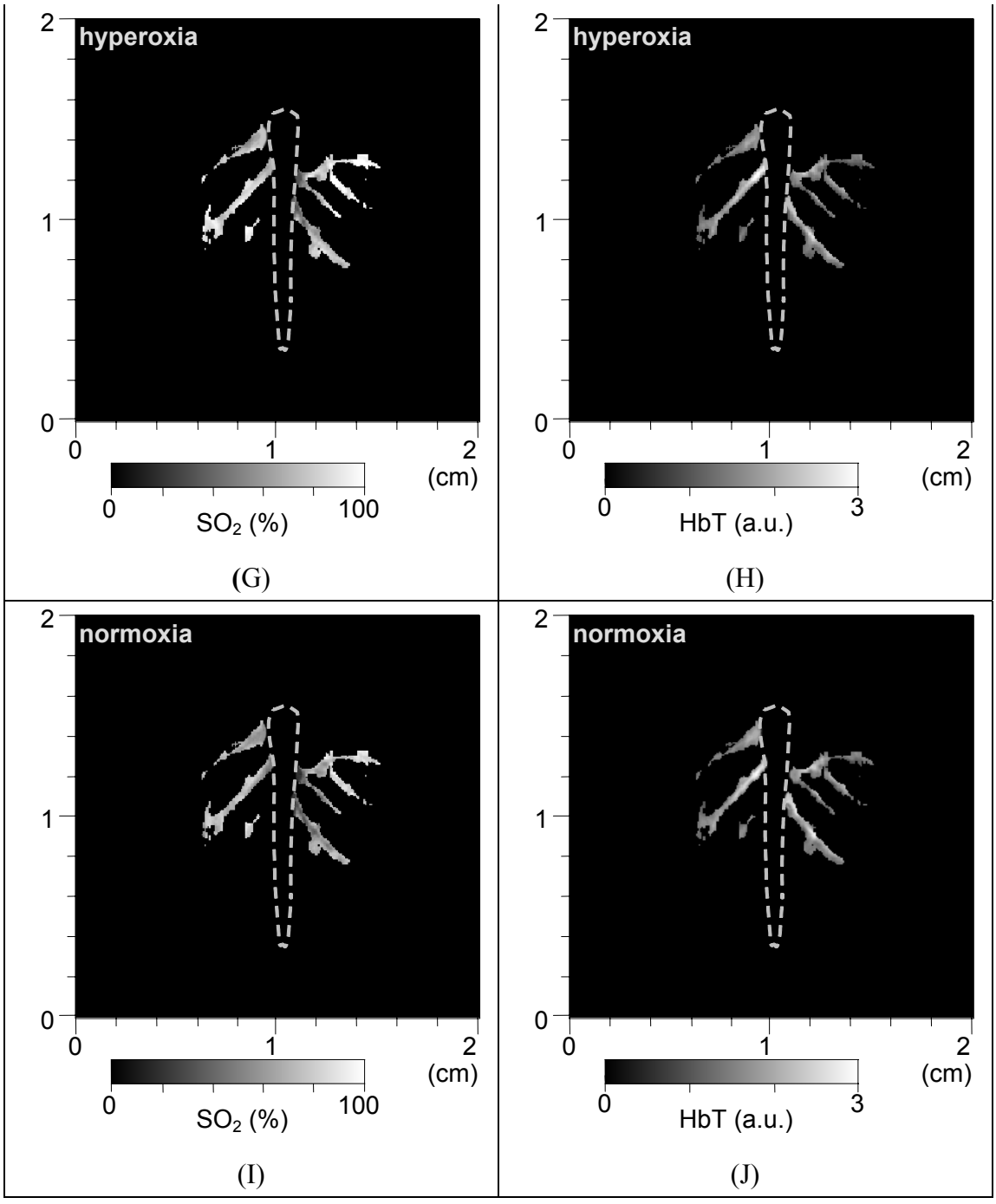

Figure 16 continued.

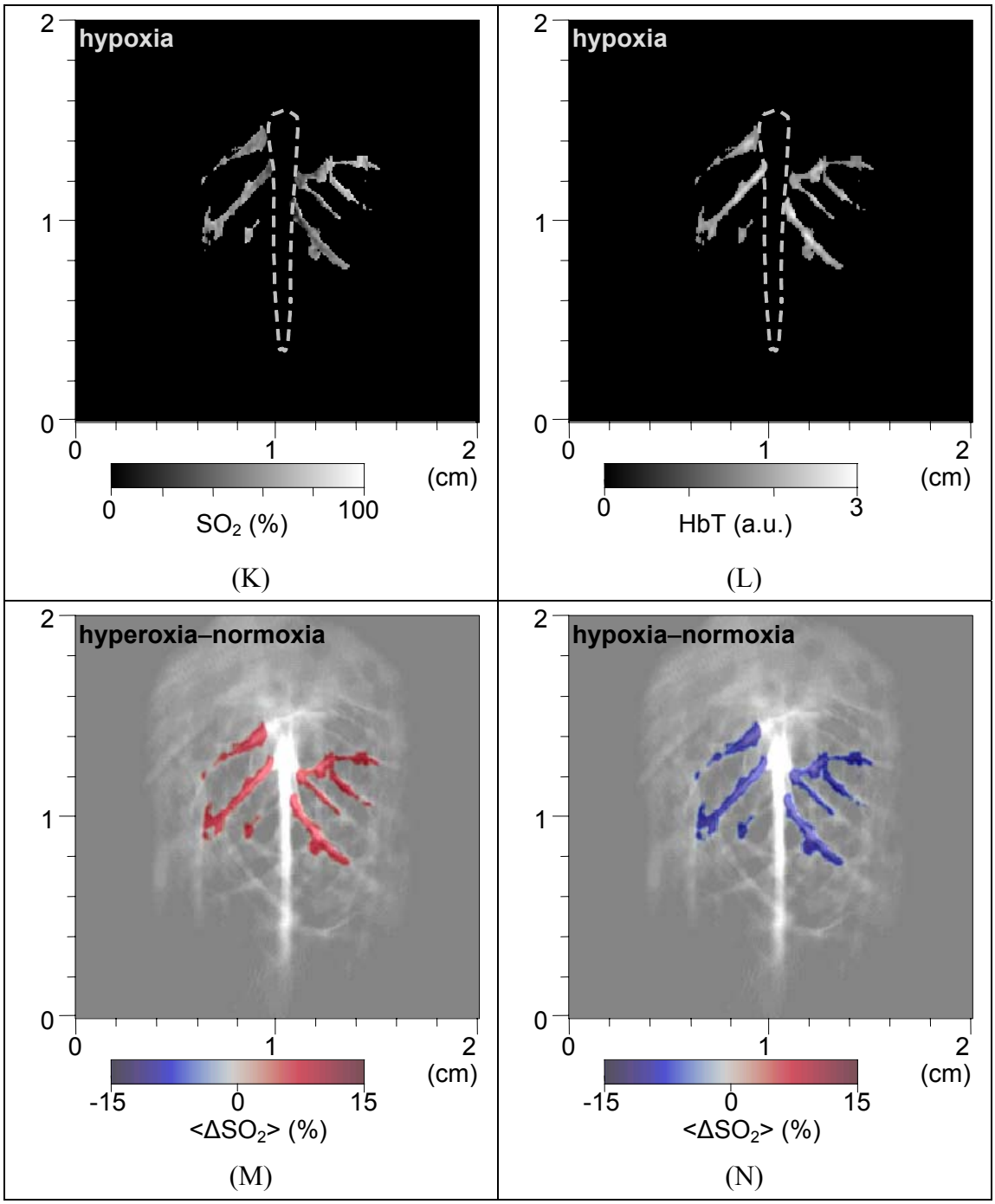

Figure 16 continued.

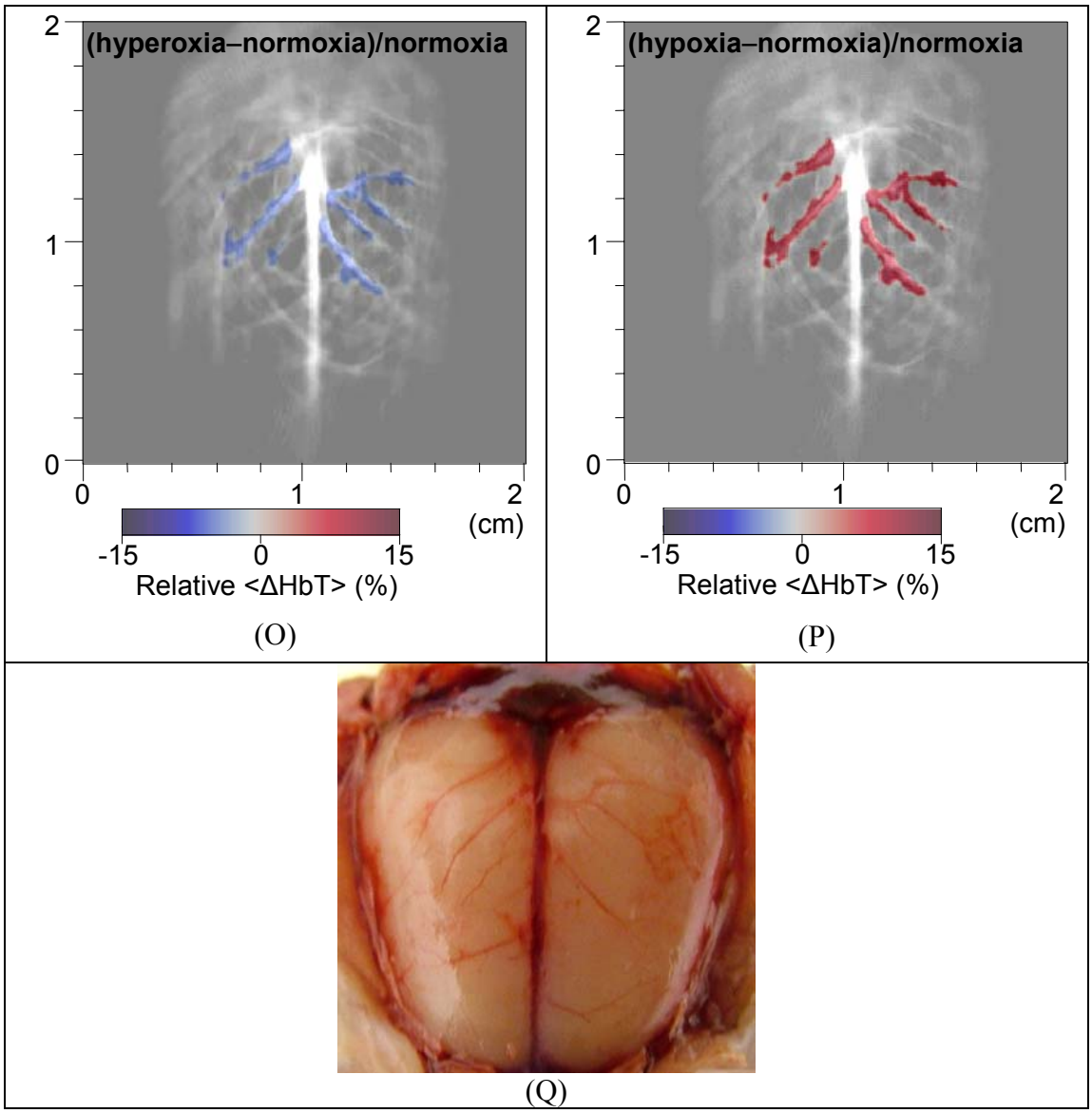

Figure 16 continued.

4.3.8 Conclusion

This study demonstrates the feasibility of multi-wavelength laser-based spectroscopic PAT for functional imaging and quantification of cerebral hemoglobin concentration and hemoglobin oxygenation non-invasively through the skin and skull. With much improved spatial resolution compared to NIRS, PAT can assess functional parameters and changes in localized areas in intact brain quantitatively or qualitatively. The PAT technique described here will potentially reveal important new insights into cerebrovascular physiology and brain function that are of great significance to the neuroscience community.

In order to investigate hemodynamics and oxygen metabolism in the brain in great detail, further improvements are needed. First, the optical properties of skin, skull and brain tissues as functions of wavelength that might affect the distribution of optical energy in the brain need to be studied. Second, 3-D brain imaging implemented by 3-D signal acquisition needs be applied because it can improve the depth resolution and hence improve the accuracy of functional measurements. Third, the application of an ultrasonic transducer array for signal acquisition instead of the single-element transducer will not only enable real-time imaging but also effectively avoid errors caused by the instability of laser energy and motions of the animals. Finally, accurate and absolute quantification of blood oxygenation is possible when photoacoustic measurements at more wavelengths are performed to eliminate the impact brought by other insignificant chromophores, such as cytochrome oxidase and water. As for the acoustic distortion induced especially by the skull, it should have no noticeable effect on the measurement of blood oxygenation because it does not change the relative intensities of photoacoustic signals generated at different wavelengths. To translate this PAT technique to clinical settings for human brains, NIR light between 700 nm to 900 nm will be applied, which has been proved feasible with our other functional imaging experiments on rat brains.

CHAPTER IV

PAT BASED ON EXTRINSIC CONTRAST

1. Significance of Molecular Imaging

In the past decades, the introduction of various powerful techniques, such as CT and MRI, allowed visualization of structures and function in biological tissues with exquisite detail. These techniques for medical imaging at tissue level contributed tremendously to many areas of medicine, including diagnostic imaging, preoperative evaluation, and therapeutic monitoring. Despite the years of effort, however, structural imaging at tissue level is insensitive for the detection of pre-cancer neoplasis, tissue metabolism, and other localized functional signals without gross structural changes in organs.

Emerging functional imaging at molecular and cellular level rather than gross level is regarded widely as the next stage of medical imaging. Molecular imaging is broadly defined as the characterization and measurement of biological processes in living animals and humans at the cellular and molecular level using remote imaging detectors. The developments in molecular science extended the horizons of non-invasive medical imaging from gross anatomical descriptions to functional cellular and biochemical information. Methods of molecular imaging facilitate not only the diagnosis of disorders, but also the non-invasive monitoring of therapeutic efficacy. Most recent advances in this field allow the characterization and identification of target tissues for gene therapy.[64,65]

2. Current Molecular Imaging Techniques

The development of reporter probes and imaging equipments is essential to realize methodologies that can monitor complex processes in living tissues at molecular and cellular level. Molecular targeting is defined as the specific concentration of a diagnostic tracer or therapeutic agent by virtue of its interaction with a molecular species that is distinctly present or absent in a disease state.[66] Agents, such as proteins, antibodies, peptides, glucose and drugs, can be aimed at molecular targets, such as tumor and nerve cell receptors. Recently, dedicated molecular imaging equipments based on

techniques such as PET, single photon emission computed tomography (SPECT), ultrasonic imaging, MRI, as well as optical imaging have been developed.

The introduction of [F-18]-fluorodeoxyglucose to PET in 1976 as a molecular imaging technique has shown the power of this approach.[67] Since then, PET and SPECT have become important clinically in diagnosis and therapy monitoring, and now play a significant role in imaging gene expression using diverse reporter genes and reporter probes.[68, 69] However, the high cost associated with the PET or SPECT setup is prohibitive for many institutions and clinics. Moreover, the images acquired by these techniques have limited resolution and hence contain little anatomical information. Therefore, the identification of regions of tracer uptake based on PET or SPECT image is difficult without enhancement from other techniques.

Contrast-enhanced ultrasound, a novel imaging technique that combines ultrasound with acoustic contrast agents, will likely expand beyond perfusion imaging. There has been considerable progress in the past few years in the development of targeting microbubbles that attach to specific markers of diseases while providing extra contrast.[70] The generation of acoustic signals by microbubbles results mainly from their oscillation in the ultrasound field. Ultrasonic imaging of targeting microbubbles is facing two major challenges, including (1) whether microbubbles in target areas can generate acoustic signals strong enough for clinical detection, and (2) how to differentiate signals from retained microbubbles from those generated by freely circulating microbubbles.

Recently, MRI based on a variety of targeting contrast agents has been explored for molecular imaging, e.g. hepatic asialoglycoprotein receptor imaging,[71] antibody-targeted MRI,[72] pancreatic secretin receptor imaging,[73] and high-affinity folate receptor imaging.[74] The advantage of MRI in molecular imaging is its high spatial resolution. The major challenge to MRI is its relative insensitivity to contrast agents compared to other molecular imaging modalities, e.g. nuclear and NIR optical imaging techniques are 10^4~10^6 times more sensitive for probe detection than MRI.

The high sensitivity and specificity of optical imaging modalities aided by contrast agents parallel those of nuclear imaging and enable the visualization of living tissues in organs such as brain at molecular and cellular level without the undesirable effect of ionizing radiation. Optical contrast agents can be small, allowing delivery to any

target of specific tissue site or cell region. Conjugating optical contrast agents, such as cyanine dye or nanoparticles, to specific bioactive materials is one way to obtain tissue-specific or molecular information.[75,76] For example, FDA-approved indocyanine green (ICG), in combination with NIR techniques, is employed widely in clinical applications such as cardiac output monitoring,[77] hepatic function study,[78] angiography in ophthalmology,[79] and tumors detection.[80] Fluorescent proteins including green fluorescent protein (GFP) and red fluorescent protein (RFP) represent a certain class of imaging marker genes with optical signatures.[81,82] However, optical-based molecular imaging modalities, whether diffuse optical tomography, fluorescence imaging, or other microscopies, cannot provide high resolution images of subsurface tissues because of the strongly scattering nature of light in biological tissues.

3. Photoacoustic Imaging of Optical Contrast Agents

Optical contrast agents have been widely explored in the past years, and some of them have already been applied in detection of and therapy for disorders. For example, cardiac output, liver function, lung blood flow, brain blood flow, and retinal blood flow/transparent structure have been measured *in vivo* or *ex vivo* using optical dyes (e.g., U.S. Pat. No. 5,494,031). In these examples, contrast agents were used to measure bodily functions such as blood flow or enzymatic clearance from bloodstream. More recently, new optical dyes have been reported that may be applied in real-time optical localization and targeting (e.g., U.S. Pat. No. 5,672,333, U.S. Pat. No. 5,698,397, WO 97/36619, WO 98/48838). These dyes are useful for microscopy *in vitro* or *in vivo*, and some have multi-modality functionality for both MRI and optical imaging. Examples of optical contrast agents include isosulfan blue, cyanine dye, quantum dots and methyl red dye.

Since the contrast of photoacoustic imaging mainly comes from the differential optical absorptions in biological tissues, most of the absorbing dyes and nanoparticles that have been used in optical imaging and therapy can be applied to PAT. In this study, distribution of NIR absorptions in biological tissues enhanced by an ICG-based optical contrast agent was imaged with the photoacoustic modality. With this technique, we successfully achieved non-invasive photoacoustic angiography—mapping of the vasculature—in rat brains *in vivo*. The dynamic concentration of this contrast agent in

brain blood after intravenous injection was also studied. Our preliminary studies proved that photoacoustic imaging of exogenous contrast agents had high sensitivity. By employing PAT with NIR light, we have successfully imaged the dynamic distribution of the ICG-based optical contrast agent in the circulatory systems of rat brains at a concentration of ~10 μM. We expect that probes in conjugation with ICG with a concentration at an order of 1 μM can be monitored by PAT using multiple wavelengths or background subtraction.

3.1 Method

The tunable dye laser pumped by the Nd:YAG laser was employed to provide light pulses at 805-nm wavelength. The incident energy density of the laser beam was controlled to <2 mJ/cm^2 on the surface of the rat head, which induced a temperature rise in the brain vessels estimated to be <3 mK. The 10 MHz XMS-310 ultrasonic transducer was used to detect the photoacoustic signals. Sprague Dawley rats (~150 g, Charles River Breeding Laboratories) were employed in this experiment.

With our current imaging system, the acquisition of photoacoustic signals is realized through a circular scan of a single-element transducer. Therefore, the data acquisition is slow. The image obtained by this setup represents a distribution of the averaged optical absorption during the period of data acquisition. In this case, an applied contrast agent with a prolonged clearance time benefits the acquisition of imaging signals, especially when several images need to be acquired after the intravenous injection. When an ultrasonic transducer array, instead of a single-element transducer, is adopted in the future, this technique will provide real-time and more accurate quantitative monitoring of a contrast agent distribution in biological tissues.

In order to prolong the circulation of ICG in the blood, polyethylene glycol (PEG),[83] an FDA approved polymer with the structure $(-CH_2CH_2O-)_n$, was adopted to stabilize ICG. This PEG conjugate of ICG (ICG-PEG) with a high absorption near 805-nm wavelength [see Fig. 17(A)] was used as a contrast agent for the first time in photoacoustic imaging. The ICG-PEG in PBS buffer was reconstituted with distilled water (pH=7.4; concentration=3.2×10^{-4} M) and then injected intravenously via the tail vein at a dosage of 0.25 ml/100 g body weight, which led to an estimated ICG

concentration of ~1×10^{-5} M in the blood. With this ICG-PEG dosage and the applied laser energy density in this experiment, the magnitude of the photoacoustic signals received by the ultrasonic transducer was of the order of 10 μV. Considering the 60-μm resolution that can be achieved by this imaging system with the 10 MHz XMS-310 transducer,[51] the number of molecules in the 60 μm×60 μm×60 μm resolvable volume was ~2 fmol, which represented an underestimate of the sensitivity of this imaging system to ICG contrast agents.

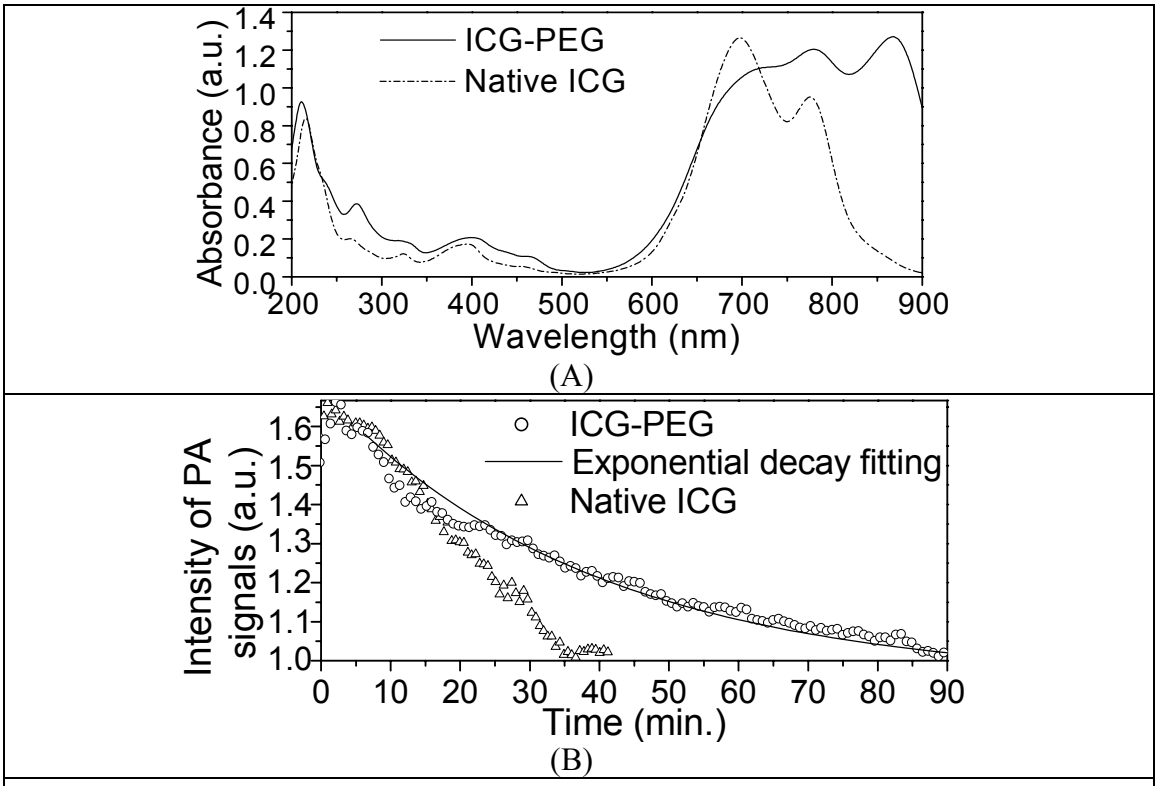

Fig. 17. Absorption and clearance of ICG-based contrast agents. (A) The absorption spectra of ICG-PEG and native ICG. (B) Intensity of the photoacoustic signals from the median fissure of the rat brain as a function of time after the intravascular injection of ICG-PEG (circles) or native ICG (triangles), which is normalized to the initial intensity of the photoacoustic signals before the injection.

By observing the changes in the intensity of the photoacoustic signals from the brain vessels, we studied the time-dependent variation of absorption in the brain blood attributable to the contrast agent [see Fig. 17 (B)]. The results represent the clearance profile of the dye from the circulatory system of the rat, where the ICG-PEG shows an

obviously slower clearance than the native ICG. With the applied dosage, ICG-PEG increases the absorption of blood in the rat median fissure up to 67%.

3.2 Contrast-enhanced PAT of rat brains in situ

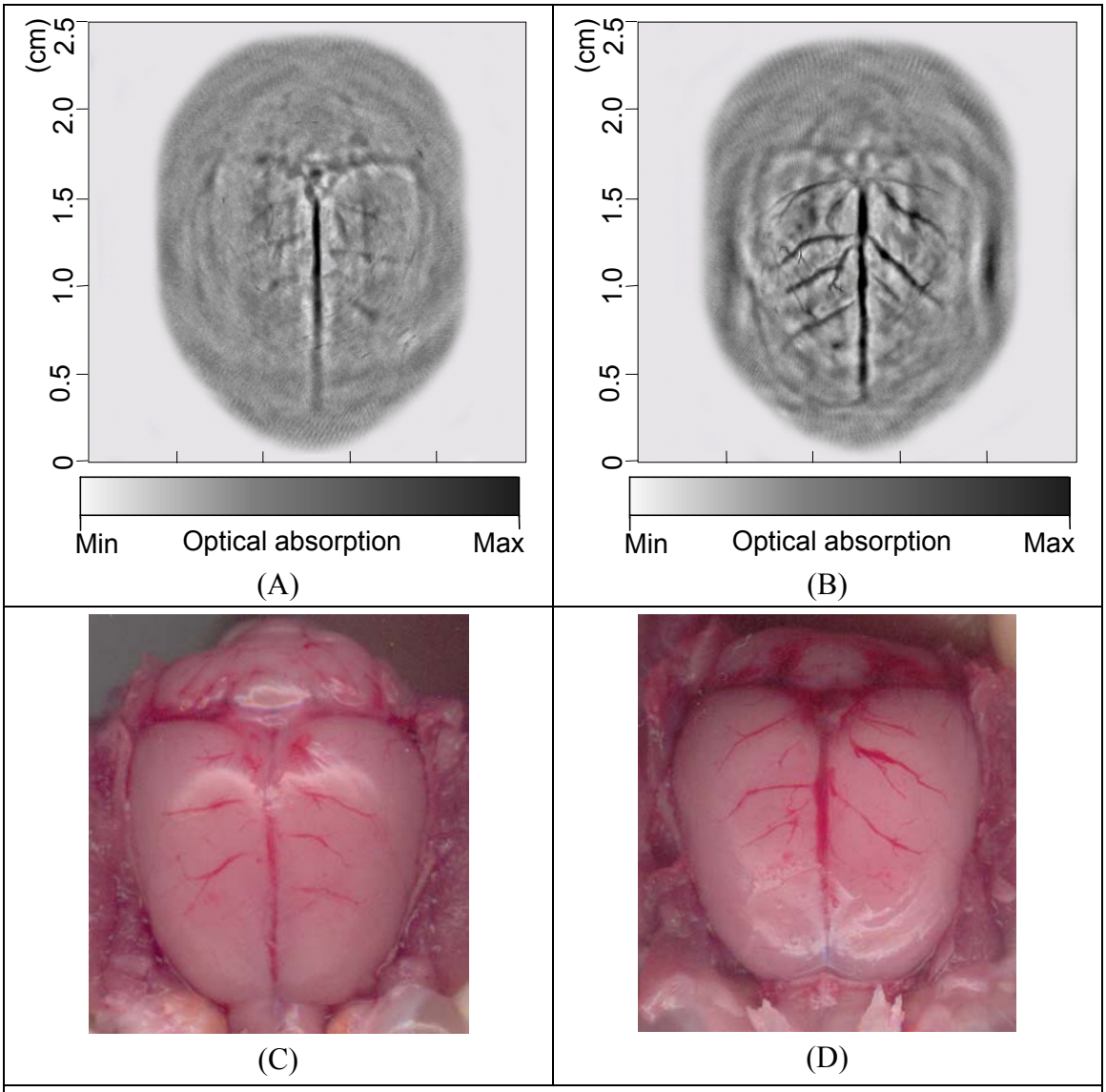

Fig. 18. Non-invasive photoacoustic angiography in rat brains *in situ*. (A) and (B), *In situ* photoacoustic images of rat brains based on intrinsic optical contrast and extrinsic optical contrast (ICG-PEG) at 805-nm wavelength, respectively. (C) and (D), Open-skull photographs of the cortical vascular distributions in rat brains corresponding to the images in (A) and (B), respectively.

Photoacoustic angiographs of rat brains *in situ* based on intrinsic and extrinsic optical contrasts were compared to verify the improvement in imaging quality that was brought about by the contrast agent (see Fig. 18). Brain image (A) was obtained from a sacrificed rat without contrast enhancement, while brain image (B) was obtained from a rat sacrificed after the intravenous injection of ICG-PEG. With the contrast enhancement, image (B) maps the brain vessels clearly with higher contrast.

3.3 Contrast-enhanced PAT of rat brains in vivo

ICG-PEG was also applied to non-invasive photoacoustic angiography in rat brains *in vivo* (see Fig. 19). After the experiment, the rat recovered normally without noticeable health problems. Compared with the reference image in Fig. 19(A), the image in Fig. 19(B), obtained after the intravenous injection of ICG-PEG, represents a clearer map of the brain vascular branches that matches well with the anatomical photograph [see Fig. 19(B)]. The reference image in Fig. 19(A) is subtracted from the contrast-enhanced image in Fig. 19(B). The differential image in Fig. 19(C) depicts the distribution of differential optical absorptions in the rat brain that is attributable to the intravenously injected contrast agent. This subtraction reduces the background and further enhances the contrast of blood vessels in the rat brain. Some detailed brain vascular structures that cannot be visualized from the image in Fig. 19(B), such as the small vessel branches identified by the arrows in the figure, are revealed by this differential image.

The current photoacoustic angiography is realized through the rotation of a single element transducer. Image obtained by this setup represents a distribution of the averaged optical absorption during the period of data acquisition. For example, the angiograph in Fig. 19(C) actually depicts the distribution of the averaged concentration of ICG-PEG in the brain blood vessels during the ~25 minutes following the injection. When an ultrasonic transducer array, instead of a single-element transducer, is adopted in the future, this technology can provide real-time and more accurate quantitative monitoring of brain hemodynamics.[20,*]

---

[*] This material has been published in *Optics Letters* 29, 730–732 (2004).

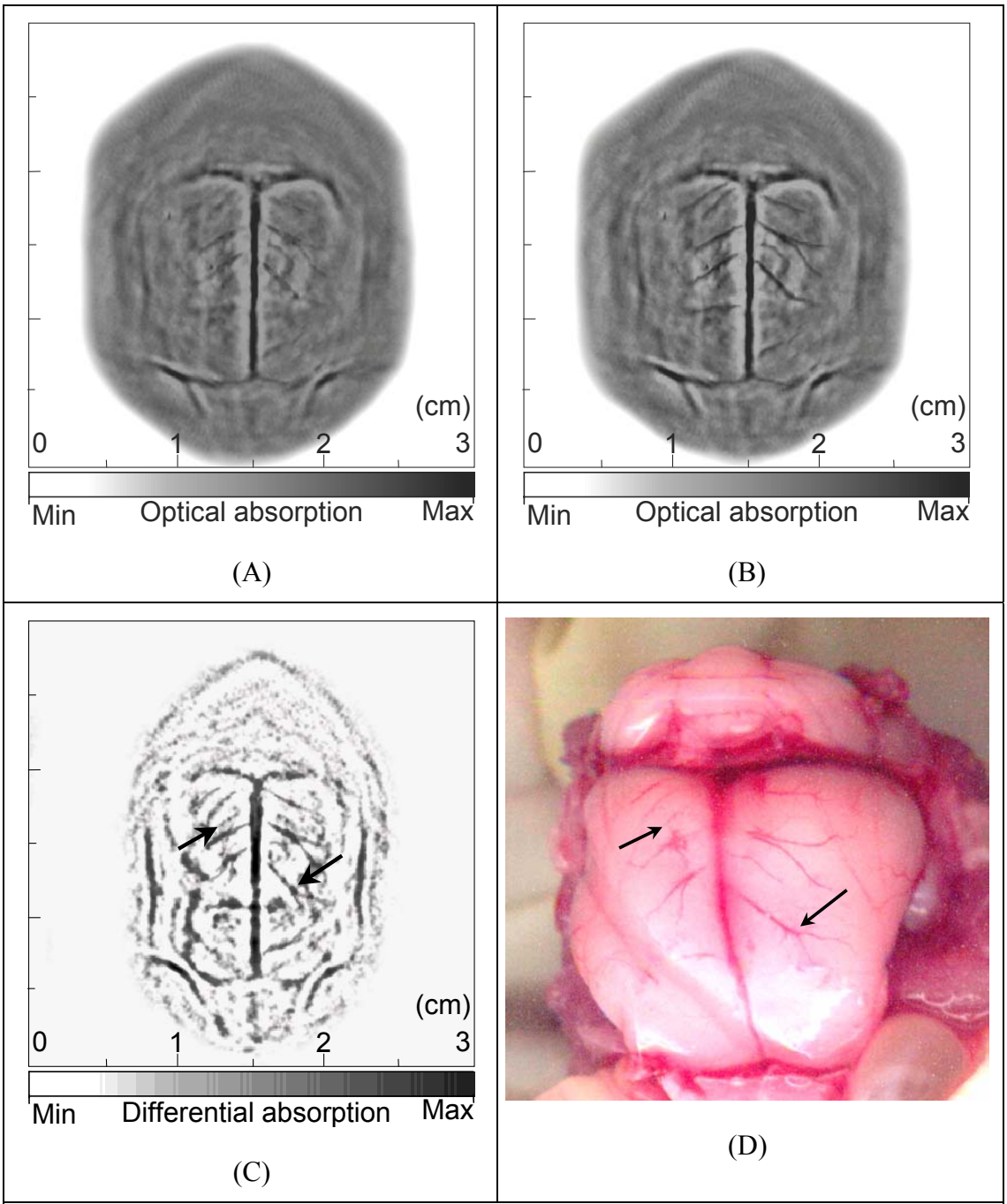

Fig. 19. Non-invasive photoacoustic angiography in a rat brain *in vivo*. (A) and (B), Photoacoustic images acquired before and after the injection of ICG-PEG, respectively. (C) Low background angiograph of the rat brain obtained by subtracting the pre-injection image from the post-injection image (C = B – A). (D) Open-skull photograph of the rat brain cerebral cortex obtained after the imaging experiment.

3.4 Dynamic imaging of contrast agent in rat brains

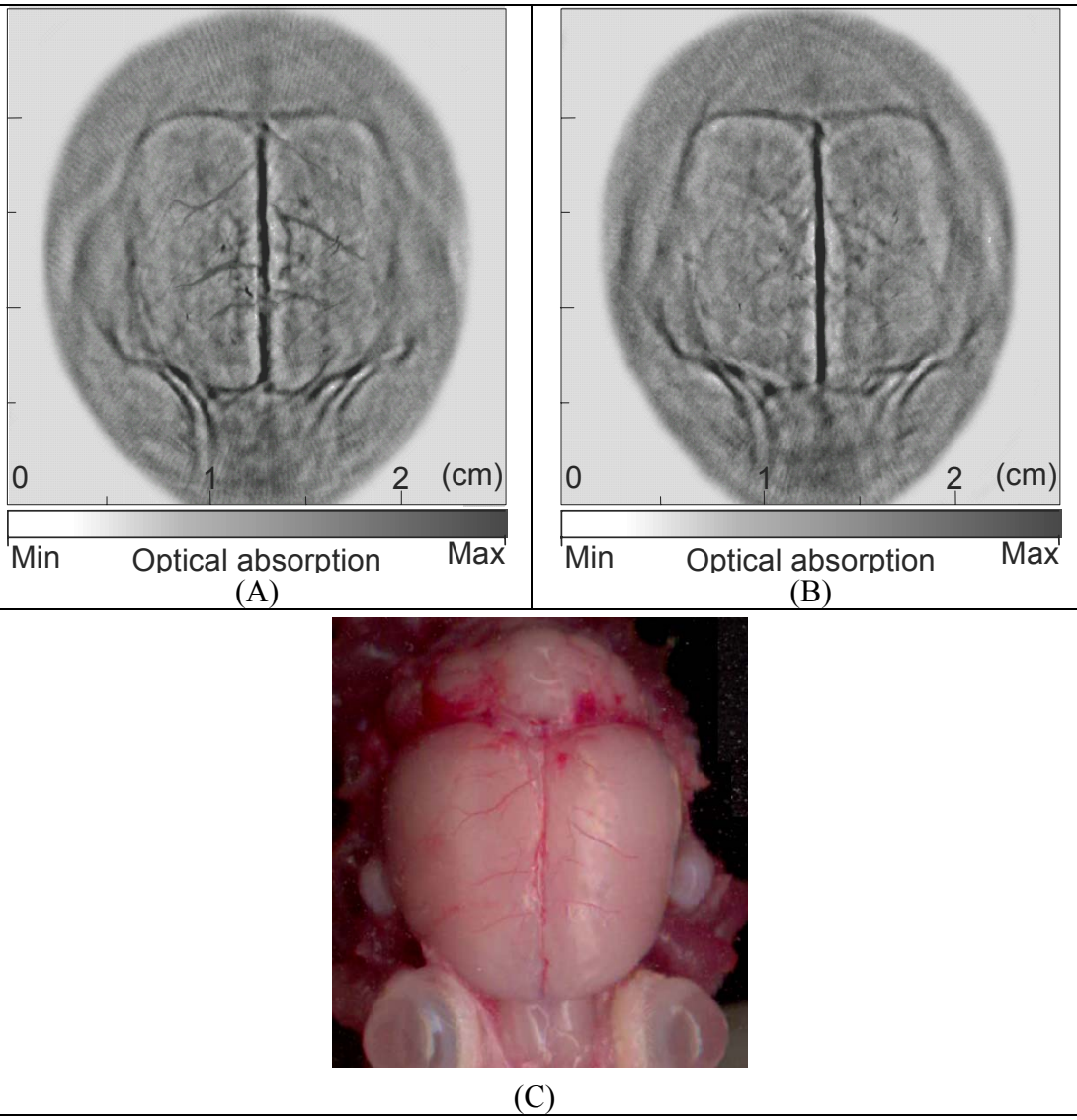

Fig. 20. Dynamic photoacoustic imaging of ICG-PEG contrast agent. The ICG-PEG in the circulatory system in a rat brain *in vivo* was imaged twice after the intravenous injection. (A) Brain image acquired during the 0 to 25 minutes after the injection. (B) Brain image acquired during the 60 to 85 minutes after the injection. (C) Open-skull anatomical photograph of the rat brain cerebral cortex obtained after the imaging experiment.

The dynamics of this contrast agent in the brain blood after the intravenous injection was also imaged (see Fig. 20). Both of the two brain images were obtained after

the intravenous injection of the contrast agent while the image in Fig. 20(A) was acquired during the 0 to 25 minutes after the injection and the image in Fig. 20(B) was acquired during the 60 to 85 minutes after the injection. Through comparison, we can see that the image quality, in other words the contrast between the blood vessels and background brain tissues, degraded as a result of the clearance of ICG-PEG from the blood.

4. Conclusion

In many circumstances, using contrast agents means the amount of physiological information to be obtained with imaging techniques can be increased significantly. PAT of ICG-PEG in the circulatory systems of rat brains proved the feasibility of this technique in imaging exogenous optical contrast agents in living tissues. This technique provides an accurate non-invasive monitoring method for fluid pathways in biological tissues, which makes this technique a powerful method for imaging pathologic tumor vessels, delineating neovascularization, and studying global and regional hemodynamic activities in the brain. Because contrast agents are expected to accumulate in neoplastic tissues or traumatized regions, this technique is promising for determining the margins of embedded tumors or bruises with a high degree of accuracy. In addition, because contrast agents can be conjugated to bioactive peptides, proteins, antibodies, hormones, drugs, or other bioactive agents, this technique can be readily extended to molecular and functional imaging for clinical applications in diagnostic imaging and therapeutic monitoring. For example, by employing high frequency ultrasonic detection and tumor-targeting optical contrast agents, this technique offers promise for imaging pathologic processes at molecular or genetic level. All of these objectives can be accomplished by virtue of the high optical contrast and high ultrasonic resolution that this technique provides.

CHAPTER V

CONCLUSION AND FUTURE WORK

1. Conclusion

My research was mainly focused on non-invasive functional photoacoustic tomography of biological tissues, especially small-animal brains. Functional PAT, as a hybrid imaging modality, combines the high contrast of optical imaging and the high resolution of ultrasonic imaging. We have achieved exciting results in our studies on PAT of small-animal brains, including 1) 2-D imaging of brain lesions; 2) 2-D imaging of brain tumors; 3) 3-D imaging of brains; 4) functional imaging of regional hemodynamics in brains induced by neuronal activities; 5) multi-wavelength spectroscopic imaging of cerebral blood oxygenation and blood volume; and 6) imaging of optical contrast agents distributed in brain vascular systems. Based on intrinsic absorption contrast of biological tissues, PAT is promising in non-invasive detection of cancers and traumas, and real-time monitoring of physiological parameters, including hemodynamics and oxygen consumption, associated with tissue function and disorders. PAT shows satisfactory sensitivity in monitoring the dynamic distributions of exogenous contrast agents, such as absorbing dyes, in living tissues. The mechanism of PAT has been validated both theoretically and experimentally. The success of the initial experiments on small animals has proved the advantages of this imaging technique.

2. Future Work

As a novel functional imaging modality, PAT has potentially wide applications. In order to translate this technique to clinical settings, further improvements need to be performed.

2.1 PAT of non-targeting contrast agents

Imaging the perfusion of non-targeting optical contrast agents is already a standard tool to study biological function and diagnose disorders in medicine today. High

absorbing contrast agents, including cyanine dyes, nanoparticles and their functional derivatives, can be employed to enhance PAT. PAT can be applied in real-time monitoring of contrast agent perfusion in vascular systems and lymphatic systems. Imaging of contrast agent perfusion in blood vessels can be applied to the assessment of acute ischaemic stroke, lesion development, thermal injury, neovascularization, tumor angiogenesis, tumor necrosis, hepatic function, and local hemodynamics. Monitoring exogenous tracers in lymphatic systems can be employed to study the lymphatic cancers and other lymphopathies. Besides intravascular imaging, PAT of exogenous contrast agents is applicable to image extravascular biological structures. For example, by observing the perfusion of optical tracers, PAT can be employed to study subarachnoid space and cerebrospinal fluid pathways.

2.2 PAT of targeting contrast agents

Optical imaging utilizing the selective uptake of contrast agents is a promising method to enable pre-cancer detection and facilitate gene therapy. In the receptor-ligand model, one (or several) signal molecule (the ligand) binds with high affinity to a specific site on a target molecule (the receptor). The key determinants of success for this type of imaging include the specificity and affinity of the receptor-ligand interaction, the density of receptors, the intensity of optical signals from these receptor-ligand pairs, and the ratio between the signals from receptor-ligand pairs and background.

Cyanine dyes are one of the most prominent classes of optical contrast agents with ideal properties for medical imaging. The optical properties of cyanine dyes are adjustable to offer high extinction coefficients ranging from the visible to the NIR. In addition, cyanine dyes can be conjugated to various specific ligands, which impart molecular specificity within the optical probes. In previous publications, cyanine dyes in conjugation with antibodies were employed to target extracellular angiogenesis-related matrix proteins[84] and enable highly sensitive oncological imaging[85]. More recently, a peptide-dye conjugation consisting of a cyanine dye and somatostatin analogyoctreotate was synthesized to serve as a contrast agent for optical tumor imaging.[86] Pyropheophorebide 2-Deoxyglucosamide, a photosensitizer targeting glucose transporter, was proved to have similar properties as ^{18}FDG and can perform as a glucose analogue to

be employed in the study of glucose metabolism in biological tissues.[87] Imaging of targeting contrast agents has many other applications including delineating gene expression[88] and monitoring drug delivering.

Different targeting optical contrast agents have already been developed and used for many years in molecular biology community as tracers. Among them, cyanine dyes, nanoparticles, and other high absorbing contrast agents can be readily employed in functional photoacoustic imaging at molecular and cellular level. PAT technique can be applied to these established models using the developed targeting contrast agents mentioned above. Also, specially designed photoacoustic contrast agents with both high absorption and high thermal-acoustic conversion efficiency can be explored. Due to the high resolution of photoacoustic technique, PAT has potential to provide better sensitivity and more anatomical information than traditional optical techniques and hence is potentially more suitable for molecular imaging.

2.3 PAT of function and disorders

PAT can be applied in real-time functional monitoring of physiological activities and disorders. For example, in the detection and study of tumors, parameters that can be evaluated include tumor angiogenesis, tumor necrosis, tumor oxygenation, and other functional changes in affected organs and adjacent areas. In the imaging of traumas, parameters that can be evaluated include anatomical location of trauma, size and extension of trauma, and functional and structural changes in affected and adjacent areas: e.g., blood oxygenation, tissue ischemia and malacia. The ability of PAT to access brain activities opens up a new window to study the physiological function and disorders of the brain.

2.4 High quality real-time functional PAT system

Although PAT on small-animal models has been validated successfully, more work needs to be fulfilled to develop high quality real-time functional PAT systems for clinical applications.

Current PAT system is based on the scan of a single element transducer. The signal acquisition is slow (~25 min per image). Therefore, quick functional changes in living tissues cannot be visualized by this system and the motion effects during the *in vivo* imaging cannot be avoided. In order to enable real-time imaging, an ultrasonic transducer array (circular array or semi-spherical array) needs to be adopted for signal acquisition. After that, the imaging speed for PAT is only limited by the signal/noise ratio. When the signal/noise ratio is high enough, a single laser pulse will enable a 2-D or 3-D image of a biological sample with satisfactory imaging quality.

Current PAT modality is based on several assumptions including 1) the light energy is homogeneously distributed in the imaging plane; and 2) the effect of acoustic heterogeneity in biological tissues, such as the discontinuity of acoustic speed and acoustic impedance, can be neglected. In order to achieve higher accuracy, the imaging reconstruction for PAT needs to be modified. Through Monte Carlo simulation, the inhomogeneous distribution of optical energy in biological tissues will be compensated. The distortion of photoacoustic waves induced by acoustic heterogeneity can be studied both theoretically and experimentally.

2.5 Functional PAT for humans

Although PAT was studied and explored on small animals first, this technique can potentially be applied to human organs, such as human brains. In order to fulfill this goal, electromagnetic sources with longer wavelengths, such as NIR light and radio-frequency microwave[89-91], will be adopted. Employing an ultrasonic detector(s) with a wide detection bandwidth, PAT is potentially capable of visualizing anatomical information and functional activities in human brain cortex. Because of the high sensitivity of PAT to both blood oxygenation and blood flow, this technique will contribute to the management of many life-threatening illnesses, including severe traumatic brain injury, ischemia, sepsis, and shock. In addition, compact PAT systems for human brains can be developed at a low cost, which enables bed-side continuous imaging and earlier initiation of monitoring in prehospital emergency vehicles. Before reaching this goal, further research of photoacoustic imaging of large animals, including cats and primates, is necessary.

REFERENCES

1. C. G. A. Hoelen, F. F. M. de Mul, R. Pongers, and A. Dekker, “Three-dimensional photoacoustic imaging of blood vessels in tissue”, Opt. Lett. **23**, 648–650 (1998).
2. A. A. Oraevsky, V. A. Andreev, A. A. Karabutov, D. R. Fleming, Z. Gatalica, H. Singh, and R. O. Esenaliev, “Laser opto-acoustic imaging of the breast: detection of cancer angiogenesis”, Proc. SPIE **3597**, 352–363 (1999).
3. G. A. Millikan, “The oximeter, an instrument for measuring continuously the oxygen saturation of arterial blood in man,” Rev. Sci. Instrum. **13**, 434 –444 (1942).
4. F. F. Jöbsis, “Noninvasive, infrared monitoring of cerebral and myocardial oxygen sufficiency and circulatory parameters,” Science **198**, 1264 –1267 (1977).
5. D. Bicout, C. Brosseau, A. S. Martinez, and J. M. Schmitt, “Depolarization of multiply scattered waves by spherical diffusers: influence of the size parameter,” Phys. Rev. E **49**, 1767–1770 (1994).
6. J. R. Mourant, M. Canpolat, C. Brocker, O. Esponda-Ramos, T. M. Johnson, A. Matanock, K. Stetter, and J. P. Freyer, “Light scattering from cells: the contribution of the nucleus and the effects of proliferative status,” J. Biomed. Opt. **5**, 131–137 (2000).
7. J. R. Mourant, I. J. Bigio, J. Boyer, R. L. Conn, T. Johnson, and T. Shimada, “Spectroscopic diagnosis of bladder cancer with elastic light scattering,” Lasers Surg. Med. **17**, 350–357 (1995).
8. G. J. Brakenhoff, P. Blom, and P. Barends, “Confocal scanning light-microscopy with high aperture immersion lenses,” J. Micros.–Oxford **117**, 219–232 (1979).
9. J. G. White and W. B. Amos, “Confocal microscopy comes of age,” Nature **328**, 183–184 (1987).
10. D. Huang, E. A. Swanson, C. P. Lin, J. S. Schuman, W. G. Stinson, W. Chang, M. R. Hee, T. Flotte, K. Gregory, C. A. Puliafito, and J. G. Fujimoto, “Optical coherence tomography,” Science **254**, 1178–1181 (1991).

11. S. Jiao and L.-H. Wang "Two-dimensional depth-resolved Mueller matrix of biological tissue measured with double-beam polarization-sensitive optical coherence tomography," Opt. Lett. **27**, 101–103 (2002).
12. B. Das, K. Yoo, and R. R. Alfano, "Ultrafast time gated imaging," Opt. Lett. **18**, 1092–1094 (1993).
13. J. C. Hebden and D. J. Delpy, "Enhanced time-resolved imaging with a diffusion model of photon transport," Opt. Lett. **9**, 311–313 (1994).
14. R. A. Kruger, D. R. Reinecke, and G. A. Kruger, "Thermoacoustic computed tomography–technical considerations," Med. Phys. **26**, 1832–1837 (1999).
15. R. O. Esenaliev, A. A. Karabutov, and A. A. Oraevsky, "Sensitivity of laser opto-acoustic imaging in detection of small deeply embedded tumors," IEEE J. Sel. Top. Quant. **5**, 981–988 (1999).
16. K. P. Köstli, D. Frauchiger, J. J. Niederhauser, G. Paltauf, H. P. Weber, and M. Frenz, "Optoacoustic imaging using a three-dimensional reconstruction algorithm," IEEE J. Sel. Top. Quant. **7**, 918–923 (2001).
17. X. Wang, Y. Xu, M. Xu, S. Yokoo, E. S. Fry, and L.-H. Wang, "Photoacoustic tomography of biological tissues with high cross-section resolution: reconstruction and experiment," Med. Phys. **29**, 2799–2805 (2002).
18. X. Wang, Y. Pang, G. Ku, X. Xie, G. Stoica, and L. V. Wang, "Non-invasive laser-induced photoacoustic tomography for structural and functional imaging of the brain *in vivo*," Nat. Biotechnol. **21**, 803–806 (2003).
19. X. Wang, Y. Pang, G. Ku, G. Stoica, and L. V. Wang, "Three-dimensional laser-induced photoacoustic tomography of the mouse brain with the skin and skull intact," Opt. Lett. **28**, 1739–1741 (2003).
20. X. Wang, G. Ku, M. A. Wegiel, D. J. Bornhop, G. Stoica, and L. V. Wang, "Noninvasive photoacoustic angiography of animal brains in vivo with near-infrared light and an optical contrast agent," Opt. Lett. **29**, 730–732 (2004).
21. L.-H. Wang, S. L. Jacques, and X.-M. Zhao, "Continuous-wave ultrasonic modulation of scattered laser light to image objects in turbid media," Opt. Lett. **20**, 629–631 (1995).

22. L.-H. Wang, “Mechanisms of ultrasonic modulation of multiply scattered coherent light: an analytic model,” Phys. Rev. Lett. **87**, 043903-(1–4) (2001).
23. M. Xu and L.-H. Wang, “Time-domain reconstruction for thermoacoustic tomography in a spherical geometry,” IEEE T. Med. Imaging **21**, 814–822 (2002).
24. R. O. Esenaliev, F. K. Tittel, S. L. Thomsen, B. Fornage, C. Stelling, A. A. Karabutov, and A. A. Oraevsky, “Laser optoacoustic imaging for breast cancer diagnostics: limit of detection and comparison with x-ray and ultrasound imaging,” Proc. SPIE **2979**, 71–82 (1997).
25. V. G. Andreev, A. A. Karabutov, and A. A. Oraevsky, “Detection of ultrawide-band ultrasound pulses in optoacoustic tomography,” IEEE T. Ultrason. Ferr. **50**, 1383–1390 (2003).
26. A. Beenen, G. Spanner, and R. Niessner, “Photoacoustic depth-resolved analysis of tissue models”, Appl. Spectrosc. **51**, 51–57, (1997).
27. A. A. Oraevsky, R. O. Esenaliev, and A. Karabutov, “Laser optoacoustic tomography of layered tissues: signal processing”, Proc. SPIE **2979**, 59–70 (1997).
28. A. A. Karabutov, E. V. Savateeva, and A. A. Oraevsky, “Imaging of layered structures in biological tissues with opto-acoustic front surface transducer”, Proc. SPIE **3601**, 284–295 (1999).
29. G. Paltauf and H. Schmidt-Kloiber, “Optical method for two-dimensional ultrasonic detection”, Appl. Phys. Lett. **75**, 1048–1050 (1999).
30. R. G. M. Kolkman, E. Hondebrink, W. Steenbergen, and F. F. M. de Mul, “In vivo photoacoustic imaging of blood vessels using an extreme-narrow aperture sensor,” IEEE J. Sel. Top. Quant. **9**, 343–346 (2003).
31. R. Fainchtein, B. J. Stoyanov, J. C. Murphy, D. A. Wilson, and D. F. Hanley, “Local determination of hemoglobin concentration and degree of oxygenation in tissue by pulsed photoacoustic spectroscopy,” Proc. SPIE **3916**, 19–33 (2000).
32. R. O. Esenaliev, I. V. Larina, K. V. Larin, D. J. Deyo, M. Motamedi, and D. S. Prough, “Optoacoustic technique for noninvasive monitoring of blood oxygenation: a feasibility study,” Appl. Optics **41**, 4722–4731 (2002).

33. A. Villringer and B. Chance, “Non-invasive optical spectroscopy and imaging of human brain function,” Trends. Neurosci. **20**, 435–442 (1997).
34. A. Grinvald, R. D. Frostig, E. E. Lieke, and R. Hildesheim, “Optical imaging of neuronal activity,” Physiol. Rev. **68**, 1285–1365 (1988).
35. R. D. Frostig, E. E. Lieke, D. Y. Ts’o, and A. Grinvald, “Cortical functional architecture and local coupling between neuronal activity and the microcirculation revealed by in vivo high resolution optical imaging of intrinsic signals,” Proc. Natl. Acad. Sci. USA **87**, 6082–6086 (1990).
36. B. A. MacVicar and D. Hochman, “Imaging of synaptically evoked intrinsic optical signals in hippocampal slices,” J. Neurosci. **11**, 1458–1469 (1991).
37. T. J. Ebner and G. Chen, “Use of voltage-sensitive dyes and optical recordings in the central nervous system” Prog. Neurobiol. **46**, 463–506 (1995).
38. G. J. Diebold, T. Sun, and M. I. Khan, in *Photoacoustic and Photothermal Phenomena III* (ed. Bicanic, D.) 263–296 (Springer-Verlag, Berlin, Heidelberg, 1992).
39. T. Sun and G. J. Diebold, “Generation of ultrasonic-waves from a layered photoacoustic source,” Nature **355**, 806–808 (1992).
40. V. E. Gusev and A. A. Karabutov, *Laser Optoacoustics* (American Institute of Physics), New York, (1993).
41. American National Standards Institute, *American National Standard for the Safe Use of Lasers. Standard Z136.1-2000* (ANSI, Inc., New York, NY, 2000).
42. B. Chance, Z. Zhuang, C. Unah, C. Alter, and L. Lipton, “Cognition-activated low-frequency modulation of light-absorption in human brain,” P. Natl. Acad. Sci. USA **90**, 3770–3774 (1993).
43. Y. Hoshi, M. Tamura, “Dynamic multichannel near-infrared optical imaging of human brain activity,” J. Appl. Physiol. **75**, 1842–1846 (1993).
44. A. Villringer, J. Planck, C. Hock, L. Schleinkofer, U. Dirnagl, “Near-infrared spectroscopy (NIRS)-a new tool to study hemodynamic-changes during activation of brain-function in human adults,” Neurosci. Lett. **154**, 101–104, (1993).

45. D. Malonek and A. Grinvald, “Interactions between electrical activity and cortical microcirculation revealed by imaging spectroscopy: implications for functional brain mapping,” Science **272**, 551–554 (1996).
46. D. E. Ingber, “Cancer as a disease of epithelial-mesenchymal interactions and extracellular matrix regulation,” Differentiation **70**, 547–560 (2002).
47. G. D. Rosen, A. G. Williams, J. A. Capra, M. T. Connolly, B. Cruz, L. Lu, D. C. Airey, K. Kulkarni, R. W. Williams (2000) The Mouse Brain Library @ www.mbl.org. Int Mouse Genome Conference 14: 166. www.mbl.org.
48. J. K. Barton, G. Frangineas, H. Pummer, and J. F. Black, “Cooperative phenomena in two-pulse, two-color laser photocoagulation of cutaneous blood vessels,” Photochem. Photobiol. **73**, 642–650 (2001).
49. P. VanderZee, M. Essenpreis, and D. T. Delpy, “Optical properties of brain tissue,” Proc. SPIE **1888**, 454–465 (1993).
50. M. Xu and L. V. Wang, “Analytic explanation of spatial resolution related to bandwidth and detector aperture size in thermoacoustic or photoacoustic reconstruction,” Phys. Rev. E **67**, 056605, 1–15 (2003).
51. G. Ku, X. Wang, G. Stoica, and L. V. Wang, “Multiple-bandwidth photoacoustic tomography,” Phys. Med. Biol. **49**, 1329–1338 (2004).
52. J. Mayhew, Y. Zheng, Y. How, B. Vuksanovic, J. Berwick, S. Askew, and P. Coffey, “Spectroscopic analysis of changes in remitted illumination: the response to increased neural activity in brain,” Neuroimage **10**, 304–326 (1999).
53. M. Nemoto, Y. Nemura, C. Sato, M. Tamura, K. Houkin, I. Koyanagi, and H. Abe, “Analysis of optical signals evoked by peripheral nerve stimulation in rat somatosensory cortex: Dynamic changes in hemoglobin concentration and oxygenation,” J. Cereb. Blood Flow Metab. **19**, 246–259 (1999).
54. G. Gratton and M. Fabiani, “Dynamic brain imaging: event-related optical signals (EROS) measures of the time course and localization of cognitive-related activity,” Psychon. Bull Rev. **5**, 535–563 (1998).

55. A. Grinvald, E. Lieke, R. D. Frostig, C. D. Gilbert, and T. N. Wiesel, "Functional architecture of cortex revealed by optical imaging of intrinsic signals," Nature **324**, 361–364 (1986).

56. M. M. Haglund, G. A. Ojemann, and D. W. Hochman, "Optical imaging of epileptiform and functional activity in human cerebral cortex," Nature **358**, 668–671 (1992).

57. M. Jones, J. Berwick, and J. Mayhew, "Changes in blood flow, oxygenation, and volume following extended stimulation of rodent barrel cortex," Neuroimage **15**, 474–487 (2002).

58. J. L. Dowling, M. M. Henegar, D. Liu, C. M. Rovainen, and T. A. Woolsey, "Rapid optical imaging of whisker responses in the rat barrel cortex," J. Neurosci. Meth. **66**, 113–122 (1996).

59. R. J. Gerrits, E. A. Stein, and A. S. Greene, "Blood flow increases linearly in rat somatosensory cortex with increased whisker movement frequency," Brain Res. **783**, 151–157 (1998).

60. A. Mayevsky and B. Chance, "Intracellular oxidation-reduction state measured insitu by a multichannel fiberoptic surface fluorometer," Science **217**, 537–540 (1982).

61. B. Chance, E. Borer, A. Evans, G. Holtom, J. Kent, M. Maris, K. Mccully, J. Northrop, and M. Shinkwin, "Optical and nuclear-magnetic-resonance studies of hypoxia in human tissue and tumors," Ann. NY Acad. Sci. **551**, 1–16 (1988).

62. S. S. Kety and C. F. Schmidt, "The effects of altered arterial tensions of carbon dioxide and oxygen on cerebral blood flow and cerebral oxygen consumption of normal young men," J. Clin. Invest. **27**, 484–491 (1948).

63. T. Q. Duong, C. Iadecola, and S. G. Kim, "Effect of hyperoxia, hypercapnia, and hypoxia on cerebral interstitial oxygen tension and cerebral blood flow," Magnet. Reson. Med. **45**, 61–70 (2001).

64. C. Bremer and R. Weissleder, "Molecular imaging–in vivo imaging of gene expression: MR and optical technologies," Acad. Radiol. **8**, 15–23 (2001).

65. S. Bhaumik and S. S. Gambhir, “Optical imaging of renilla luciferase reporter gene expression in living mice,” P. Natl. Acad. Sci. USA **99**, 377–382 (2002).
66. S. H. Britz-Cunningham and S. J. Adelstein, “Molecular targeting with radionuclides: state of the science,” J. Nucl. Med. **44**, 1945–1961 (2003).
67. B. M. Gallagher, A. Ansari, H. Atkin, V. Casella, D. R. Christman, J. S. Fowler, T. Ido, R. R. Macgregor, P. Som, C. N. Wan, A. P. Wolf, D. E. Kuhl, and M. Reivich, “Radiopharmaceuticals .27. F-18-labelled 2-deoxy-2-fluoro-D-glucose as a radiopharmaceutical for measuring regional myocardial glucose-metabolism in vivo-tissue distribution and imaging studies in animals,” J. Nucl. Med. **18**, 990–996 (1977).
68. J. G. Tjuvajev, R. Finn, K. Watanabe, R. Joshi, T. Oku, J. Kennedy, B. Beattie, J. Koutcher, S. Larson, and R. G. Blasberg, “Noninvasive imaging of herpes virus thymidine kinase gene transfer and expression: a potential method for monitoring clinical gene therapy,” Cancer Res. **56**, 4087–4095 (1996).
69. S. S. Gambhir, J. R. Barrio, M. E. Phelps, M. Iyer, M. Namavari, N. Satyamurthy, L. Wu, L. A. Green, E. Bauer, D. C. MacLaren, K. Nguyen, A. J. Berk, S. R. Cherry, and H. R. Herschman, “Imaging adenoviral-directed reporter gene expression in living animals with positron emission tomography,” Proc. Natl. Acad. Sci. USA **96**, 2333–2338 (1999).
70. A. L. Klibanov, “Targeted delivery of gas-filled microspheres, contrast agents for ultrasound imaging,” Adv. Drug Deliv. Rev. **37**, 139–157 (1999).
71. R. Weissleder, P. Reimer, A. Lee, J. Wittenberg, and T. Brady, “MR receptor imaging: ultrasmall iron oxide particles targeted to asialoglycoprotein receptors,” AJR **155**, 1161–1167 (1990).
72. R. Weissleder, A. S. Lee, T. Shen, and T. J. Brady, “Antimyosin-labeled monocrystalline iron xoide allows detection of myocardial infarct: MR antibody imaging,” Radiology **182**, 381–385 (1992).
73. S. D. Konda, M. Aref, M. Brechbiel, and E. C. Wiener, “Development of a tumor-targeting MR contrast agent using the high-affinity folate receptor: work in progress,” Invest. Radiol. **35**, 50–57 (2000).

74. T. Shen, A. Bogdanov, A. Bogdanova, K. Poss, T. Brady, and R. Weiss-leder, "Magnetically labeled secretin retains receptor affinity to pancreas acinar cells," Bioconjug. Chem. **7**, 311–316 (1996).

75. D. J. Bornhop, C. H. Contag, K. Licha, and C. J. Murphy, "Advance in contrast agent, reporters, and detection," J. Biomed. Opt. **6**, 106–110 (2001).

76. K. Sokolov, M. Follen, J. Aaron, I. Pavlova, A. Malpica, R. Lotan, and R. Richards-Kortum, "Real-time vital optical imaging of precancer using anti-epidermal growth factor receptor antibodies conjugated to gold nanoparticles," Cancer Res. **63**, 1999–2004 (2003).

77. Y.-L. He, H. Tanigami, H. Ueyama, T. Mashimo, and I. Yoshiya, "Measurement of blood volume using indocyanine green measured with pulse-spectrometry: Its reproducibility and reliability," Crit. Care Med. **26**, 1446–1451 (1998).

78. J. Caesar, S. Shaldon, L. Chiandussi, L. Guevara, and S. Sherlock, "The use of Indocyanine green in the measurement of hepatic blood flow and as a test of hepatic function," Clin. Sci. **21**, 43–57 (1961).

79. B. F. Hochheim, "Angiography of retina with indocyanine green," Arch. Ophthalmol. **86**, 564–565 (1971).

80. M. M. Haglund, M. S. Berger, and D. W. Hochman, "Enhanced optical imaging of human gliomas and tumor margins," Neurosurgery **38**, 308–317 (1996).

81. X. Yang, H. Liu, D. Li, X. Zhou, W. C. Yung, A. E. Deans, Y. Cui, and L. Cheng, "Digital optical imaging of green fluorescent proteins for tracking vascular gene expression: feasibility study in rabbit and human cell models," Radiology **219**, 171–175 (2001).

82. A. Jr. Bogdanov, C. P. Lin, M. Simonova, L. Matuszewski, and R. Weisleder, "Cellular activation of the self-quenched fluorescent reporter probe in tumor microenvironment," Neoplasia **4**, 228–236 (2002).

83. S. Zalipsky, E. Brandeis, M. S. Newman, and M. C. Woodle, "Long circulating, cationic liposomes containing amino-PEG-phosphatidylethanolamine," FEBS Lett. **353**, 71–74 (1994).

84. D. Neri, B. Carnemolla, A. Nissim, A. Leprini, G. Querze, E. Balza, A. Pini, L. Tarli, C. Halin, P. Neri, L. Zardi, and G. Winter, "Targeting by affinity-matured recombinant antibody fragments of an angiogenesis associated fibronectin isoform," Nat. Biotechnol. **15**, 1271–1275 (1997).

85. R. Weissleder, C.-H. Tung, U. Mahmood, and A. Jr. Bogdanov, "In vivo imaging of tumors with protease-activated near-infrared fluorescent probes," Nat. Biotechnol. **17**, 375–378 (1999).

86. A. Becker, C. Hessenius, K. Licha, B. Ebert, U. Sukowski, W. Semmler, B. Wiedenmann, and C. Grotzinger, "Receptor-targeted optical imaging of tumors with near-infrared fluorescent lights," Nat. biotechnol. **19**, 327–331 (2001).

87. M. Zhang, Z. H. Zhang, D. Blessington, H. Li, T. M. Busch, V. Madrak, J. Miles, B. Chance, J. D. Glickson, and G. Zheng, "Pyropheophorbide 2-deoxyglucosamide: a new photosensitizer targeting glucose transporters," Bioconjugate Chem. **14**, 709–714 (2003).

88. U. Mahmood, C. H. Tung, Y. Tang, and R. Weissleder, "Feasibility of in vivo multichannel optical imaging of gene expression: experimental study in mice," Radiology **224**, 446–451 (2002).

89. G. Ku and L.-H. Wang, "Scanning thermoacoustic tomography in biological tissue," Med. Phys. **27**, 1195–1202 (2000).

90. M. Xu, G. Ku, and L.-H. Wang, "Microwave-induced thermoacoustic tomography using multi-sector scanning," Med. Phys. **28**, 1958–1963 (2001).

91. D. Feng, Y. Xu, G. Ku, and L.-H. Wang, "Microwave-induced thermoacoustic tomography: reconstruction by synthetic aperture," Med. Phys. **28**, 2427–2431 (2001).

APPENDIX

MONTE CARLO SIMULATION

1. Introduction

In both diagnostic and therapeutic applications of light in medicine, it is important to evaluate the optical properties of biological tissues including the absorption coefficient, scattering coefficient, refraction index and anisotropy factor. The information in these optical properties can be used to monitor tissue metabolic status or diagnose disease, for example cancers. The optical properties of a scattering medium can be measured by shining a light beam onto the medium and then analyzing the state of the diffusely reflected or transmitted light. This technique has been used to measure absorption coefficients, scattering coefficients and anisotropy factors of biological tissues or tissue phantoms. Besides these common optical properties, polarized light can provide polarization contrast that is produced by specific tissue properties, for example, chiral effect caused by glucose molecules and birefringent effect brought by collagen and muscle fibers.

The propagation of polarized light in a scattering medium is a complex process. Optical properties of the scattering medium, such as the size, the shape, and the refractive index of the scattering particles as well as the polarization state of the incident light, all play important roles. The Monte Carlo technique offers a flexible and accurate approach to solve this problem, because it can trace the detailed information in polarization propagation inside and outside a scattering medium with a complex geometry and can score multiple physical quantities simultaneously.

Employing a time-resolved Monte Carlo technique, we studied the initially polarized light propagation in scattering media made of polystyrene-microspheres solutions. Propagation and evolution of initially polarized light in scattering media containing friberous materials and chiral components were also analyzed. The theoretical study of light propagation in scattering media can help us to be familiar with light-tissue interactions. In this appendix, the theory of our Monte Carlo simulation based on the Stokes/Mueller formalism is presented.

2. Theory

2.1 Stokes vector and Mueller matrix

An optical field, **E**, can be presented in a Jones vector:

$$\mathbf{E} = \begin{bmatrix} E_x \\ E_y \end{bmatrix} = \begin{bmatrix} A_x e^{i\phi_x} \\ A_y e^{i\phi_y} \end{bmatrix}, \tag{7}$$

where E_x and E_y are complex, oscillation functions. The state of light can also be represented by a 4 by 1 Stokes vector:

$$\mathbf{S} = \begin{bmatrix} S_0 \\ S_1 \\ S_2 \\ S_3 \end{bmatrix} = \begin{bmatrix} < E_x E_x^* + E_y E_y^* > \\ < E_x E_x^* - E_y E_y^* > \\ < E_x E_y^* + E_y E_x^* > \\ < i(E_x E_y^* - E_y E_x^*) > \end{bmatrix} = \begin{bmatrix} < A_x^2 + A_y^2 > \\ < A_x^2 - A_y^2 > \\ < 2A_x A_y \cos\Delta\phi > \\ < 2A_x A_y \sin\Delta\phi > \end{bmatrix}, \tag{8}$$

where the Stokes parameters S_0 shows the total intensity; S_1 and S_2 represent the linear polarization component; S_3 represents the circular polarization component; and $\Delta\phi = \phi_x - \phi_y$. For example, the set of parameters (S_0, S_1, S_2, S_3) for natural light in normalized representation is (1,0,0,0). If the light is horizontally polarized without vertical component, then its normalized representation is (1,1,0,0). For completely polarized light, we have

$$S_0^2 = S_1^2 + S_2^2 + S_3^3 . \tag{9}$$

For partially polarized light, its degree of polarization (DOP), degree of linear polarization (DOLP) and degree of circular polarization (DOCP) can be given by

$$\begin{cases} DOP = \dfrac{\sqrt{S_1^2 + S_2^2 + S_3^3}}{S_0} \\ DOLP = \dfrac{\sqrt{S_1^2 + S_2^2}}{S_0} \\ DOCP = \left|\dfrac{S_3}{S_0}\right| \end{cases} . \tag{10}$$

The property of an optical device can be fully expressed by a 4 by 4 Mueller matrix **M**. With the Stokes vector of the incident light, the state of light transmitted through the optical device, can be obtained by

$$\mathbf{S}_{out} = \mathbf{M}\mathbf{S}_{in} . \tag{11}$$

2.2 Single-scattering event

2.2.1 Single-scattering geometry

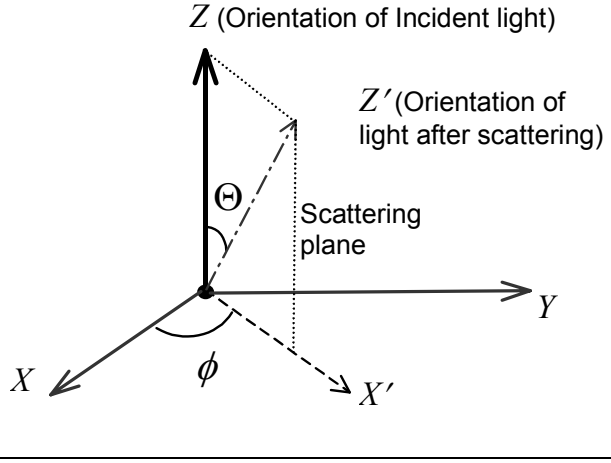

Fig. 21. Geometry of a single-scattering event.

Before the study of polarization propagation in a scattering medium, we analyzed the single scattering of light by a spherical scattering particle. The scattering geometry is shown in Fig. 21, where $\phi \in [0, 2\pi)$ is the azimuthal angle and $\Theta \in [0, \pi]$ is the deflection angle. Firstly, the coordinate system (X, Y, Z) rotates a ϕ angle from the X-axis toward the Y-axis around the Z-axis, which leads to a coordinate system (X', Y', Z). The plane determined by the X-axis and the Z-axis is named as reference plane; while the plane determined by the X'-axis and the Z-axis is named as scattering plane. Then the Z-axis, after a rotation of a Θ angle toward the X'-axis in the scattering plane, becomes the Z'-axis. Once the Θ and the ϕ are known, the orientation of light propagation after the scattering (Z'-axis) is determined. After this single-scattering event, the Stokes vector of the incident light will be transformed by

$$\mathbf{S}_1(\phi,\Theta) = \mathbf{M}(\Theta)\mathbf{R}(\phi)\mathbf{S}_0, \tag{12}$$

where $\mathbf{S}_0$ and $\mathbf{S}_1$ are the Stokes vectors of light before and after the single-scattering event; $\mathbf{R}(\phi)$ is the rotation matrix; and $\mathbf{M}(\Theta)$ is the single-scattering matrix.

2.2.2 Rotation matrix

The rotation matrix $\mathbf{R}(\phi)$ connects the two Stokes vectors that describe the same polarization state corresponding to the reference plane and the scattering plane, respectively. The Jones vectors of light before and after the rotation can be expressed as: $\begin{bmatrix} E_x \\ E_y \end{bmatrix}$ and $\begin{bmatrix} E_x' \\ E_y' \end{bmatrix}$, respectively. We have

$$\begin{bmatrix} E_x' \\ E_y' \end{bmatrix} = \begin{bmatrix} \cos\phi & \sin\phi \\ -\sin\phi & \cos\phi \end{bmatrix} \begin{bmatrix} E_x \\ E_y \end{bmatrix} = \vec{\mathbf{J}} \begin{bmatrix} E_x \\ E_y \end{bmatrix}. \tag{13}$$

Since Mueller matrix can be deduced from Jones Matrix by $\vec{\mathbf{M}} = \mathbf{A}(\vec{\mathbf{J}} \otimes \vec{\mathbf{J}}^*)\mathbf{A}^{-1}$, where $\mathbf{A} = \begin{bmatrix} 1 & 0 & 0 & 1 \\ 1 & 0 & 0 & -1 \\ 0 & 1 & 1 & 0 \\ 0 & i & -i & 0 \end{bmatrix}$, we can obtain the corresponding rotation Mueller matrix as:

$$\mathbf{R}(\phi) = \begin{bmatrix} 1 & 0 & 0 & 0 \\ 0 & \cos 2\phi & \sin 2\phi & 0 \\ 0 & -\sin 2\phi & \cos 2\phi & 0 \\ 0 & 0 & 0 & 1 \end{bmatrix}. \tag{14}$$

2.2.3 Single-scattering matrix and Mie theory

According to the Mie theory, the deflection angle Θ is defined as the rotation of the propagation direction (Z-axis) toward the l-axis (see Fig. 22). The electric vector before and after the scattering event can be expressed as $\begin{bmatrix} E_l \\ E_r \end{bmatrix}$ and $\begin{bmatrix} E_l' \\ E_r' \end{bmatrix}$, respectively, where Z, Z', l and l' are in the scattering plane; r is perpendicular to the scattering plane; and $\vec{r} \times \vec{l} = \vec{Z}$. The electric vector after the scattering event can be obtained by

$$\begin{bmatrix} E_l' \\ E_r' \end{bmatrix} = \begin{bmatrix} A_2 & A_3 \\ A_4 & A_1 \end{bmatrix} \begin{bmatrix} E_l \\ E_r \end{bmatrix} = \mathbf{J} \begin{bmatrix} E_l \\ E_r \end{bmatrix}. \tag{15}$$

With the Jones matrix **J**, we can obtain the Mueller matrix for a single-scattering event:

$$\mathbf{F} = \begin{bmatrix} \frac{1}{2}(M_2 + M_3 + M_4 + M_1) & \frac{1}{2}(M_2 - M_3 + M_4 - M_1) & S_{23} + S_{41} & -D_{23} - D_{41} \\ \frac{1}{2}(M_2 + M_3 - M_4 - M_1) & \frac{1}{2}(M_2 - M_3 - M_4 + M_1) & S_{23} - S_{41} & -D_{23} + D_{41} \\ S_{24} + S_{31} & S_{24} - S_{31} & S_{21} + S_{34} & -D_{21} + D_{34} \\ D_{24} + D_{31} & D_{24} - D_{31} & D_{21} + D_{34} & S_{21} - S_{34} \end{bmatrix}, \tag{16}$$

$$M_k = A_k A_k^* = |A_k|^2,$$

where $S_{kj} = S_{jk} = \frac{1}{2}(A_j A_k^* + A_k A_j^*),$

$$-D_{kj} = D_{jk} = \frac{i}{2}(A_j A_k^* - A_k A_j^*).$$

For spherical scattering particles, A_3 and A_4 in Eq. (15) equal 0. Then the single-scatteing matrix has the form of

$$\mathbf{M} = \frac{1}{2}\begin{bmatrix} |S_2|^2 + |S_1|^2 & |S_2|^2 - |S_1|^2 & 0 & 0 \\ |S_2|^2 - |S_1|^2 & |S_2|^2 + |S_1|^2 & 0 & 0 \\ 0 & 0 & S_2 S_1^* + S_1 S_2^* & -i(S_2 S_1^* - S_1 S_2^*) \\ 0 & 0 & i(S_2 S_1^* - S_1 S_2^*) & S_2 S_1^* + S_1 S_2^* \end{bmatrix}. \tag{17}$$

The detailed simulation of S_1 and S_2 can be found in the thesis of Gang Yao.

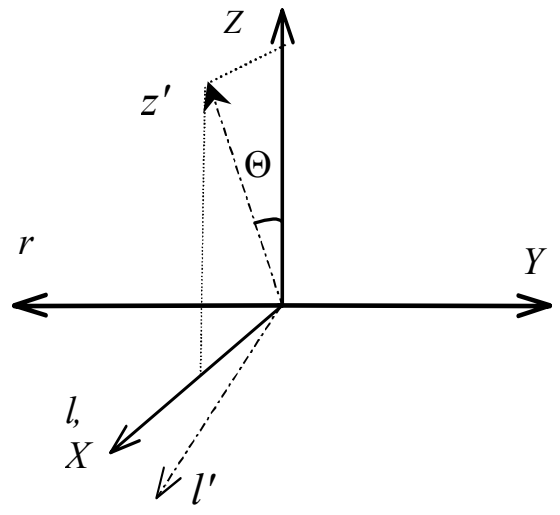

Fig. 22. Scattering in the *X*-*Y*-*Z* coordinates and the *r*-*l*-*Z* coordinates.

Now the single scattering matrix in the *X*-*Y*-*Z* coordinate system is considered, where $\vec{X} \times \vec{Y} = \vec{r} \times \vec{l} = \vec{Z}$. Before the scattering event, we have

$$\begin{bmatrix} E_x \\ E_y \end{bmatrix} = \begin{bmatrix} E_l \\ -E_r \end{bmatrix} = \begin{bmatrix} 1 & 0 \\ 0 & -1 \end{bmatrix} \begin{bmatrix} E_l \\ E_r \end{bmatrix}; \tag{18}$$

after the scattering, we have

$$\begin{bmatrix} E_x{}' \\ E_y{}' \end{bmatrix} = \begin{bmatrix} E_l{}' \\ -E_r{}' \end{bmatrix} = \begin{bmatrix} 1 & 0 \\ 0 & -1 \end{bmatrix} \begin{bmatrix} E_l{}' \\ E_r{}' \end{bmatrix}. \tag{19}$$

With the relationship

$$\begin{bmatrix} E_l{}' \\ E_r{}' \end{bmatrix} = \begin{bmatrix} A_2 & A_3 \\ A_4 & A_1 \end{bmatrix} \begin{bmatrix} E_l \\ E_r \end{bmatrix}, \tag{20}$$

we have

$$\begin{bmatrix} E_x{}' \\ E_{y'} \end{bmatrix} = \begin{bmatrix} A_2 & -A_3 \\ -A_4 & A_1 \end{bmatrix} \begin{bmatrix} E_x \\ E_y \end{bmatrix} = \mathbf{J} \begin{bmatrix} E_x \\ E_y \end{bmatrix}. \tag{21}$$

For spherical scattering particles, we have $\mathbf{J} = \begin{bmatrix} A_2 & 0 \\ 0 & A_1 \end{bmatrix}$. Therefore, when the deflection angle Θ is defined as a rotation of the *Z*-axis toward the *X*-axis, the single-scattering Mueller matrix for the *X*-*Y*-*Z* coordinate system has the form of

$$\mathbf{M}(\Theta) = \frac{1}{2} \begin{bmatrix} |S_2|^2 + |S_1|^2 & |S_2|^2 - |S_1|^2 & 0 & 0 \\ |S_2|^2 - |S_1|^2 & |S_2|^2 + |S_1|^2 & 0 & 0 \\ 0 & 0 & S_2 S_1{}^* + S_1 S_2{}^* & -i(S_2 S_1{}^* - S_1 S_2{}^*) \\ 0 & 0 & i(S_2 S_1{}^* - S_1 S_2{}^*) & S_2 S_1{}^* + S_1 S_2{}^* \end{bmatrix}, \tag{22}$$

that is the same as Eq. (17) and can be expressed simply as

$$\mathbf{M}(\Theta) = \begin{bmatrix} m_{11}(\Theta) & m_{12}(\Theta) & 0 & 0 \\ m_{12}(\Theta) & m_{11}(\Theta) & 0 & 0 \\ 0 & 0 & m_{33}(\Theta) & m_{34}(\Theta) \\ 0 & 0 & -m_{34}(\Theta) & m_{33}(\Theta) \end{bmatrix}. \tag{23}$$

The element m_{11} satisfies the normalization requirement:

$$2\pi \int_0^\pi m_{11}(\Theta) \sin(\Theta) d\Theta = 1. \tag{24}$$

We have a joint probability density function (PDF) of the deflection angle and the azimuthal angle:

$$\rho(\Theta,\phi) = m_{11}(\Theta) + m_{12}(\Theta)[S_1\cos(2\phi) + S_2\sin(2\phi)]/S_0, \tag{25}$$

which is a function of the incident Stokes vector. In our method, the deflection angle is sampled according to $m_{11}(\Theta)$ and the azimuthal angle is sampled according to

$$\rho_\theta(\phi) = \frac{1}{2\pi}\{1 + \frac{m_{12}(\Theta)}{m_{11}(\Theta)}[S_1\cos(2\phi) + S_2\sin(2\phi)]/S_0\}. \tag{26}$$

2.2.4 Transformation of local coordinate system

In the Monte Carlo simulation, for each single-scattering event, two angles—the azimuthal angle ϕ and the deflection angle Θ—are adopted to trace the propagation direction of a photon packet after the scattering. The local coordinate system also needs a transformation after the single-scattering event.

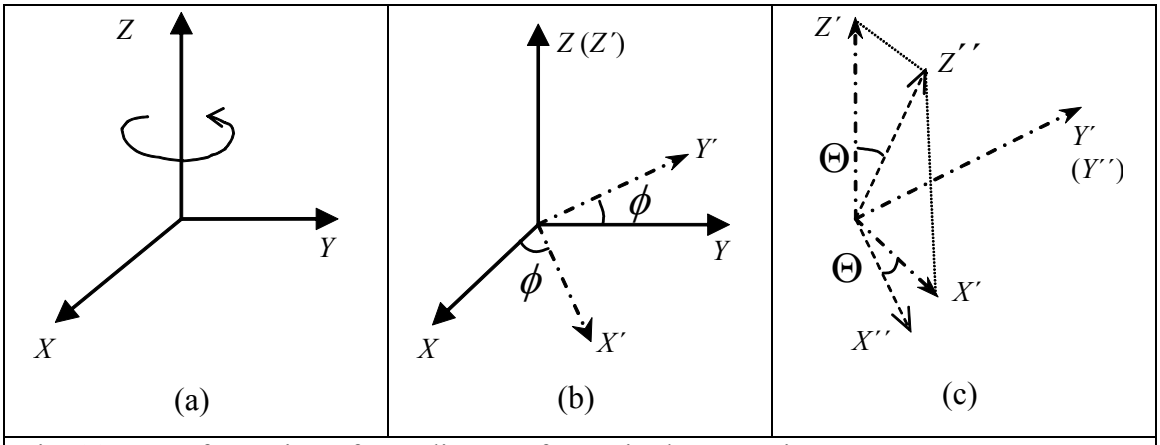

Fig. 23. Transformation of coordinates after a single-scattering event.

After two steps of rotations (see Fig. 23), we have a new local coordinate system (X'', Y'', Z'') that can be simulated by

$$\begin{bmatrix} x'' \\ y'' \\ z'' \end{bmatrix} = \begin{bmatrix} \cos\Theta & 0 & -\sin\Theta \\ 0 & 1 & 0 \\ \sin\Theta & 0 & \cos\Theta \end{bmatrix} \begin{bmatrix} \cos\phi & \sin\phi & 0 \\ -\sin\phi & \cos\phi & 0 \\ 0 & 0 & 1 \end{bmatrix} \begin{bmatrix} x \\ y \\ z \end{bmatrix} = \begin{bmatrix} \cos\Theta\cos\phi & \cos\Theta\sin\phi & -\sin\Theta \\ -\sin\phi & \cos\phi & 0 \\ \sin\Theta\cos\phi & \sin\Theta\sin\phi & \cos\Theta \end{bmatrix} \begin{bmatrix} x \\ y \\ z \end{bmatrix}. \tag{27}$$

2.3 Multiple-scattering event

The geometry of multiple-scattering events in a polystyrene-microspheres solution is shown in Fig. 24. The MC simulation that describes the multiple-scattering events of light in turbid media is based on the radiative theory, which assumes that scattering events are independent and ignores coherent effects. A narrow pencil beam propagates downward along the *Z*-axis into a plan-parallel slab of scattering medium with a thickness of *L*. The incident point is (0, 0, 0) in the laboratory coordinate system (*X*, *Y*, *Z*). Photon packets are scattered in the medium by spherical particles before exiting the upper or lower surface of the medium. At each scattering event, the scattering angles of the photon packets are selected statistically according to the Mie theory. During the propagation, the polarization evolutions of photon packets are traced through the Stokes/Mueller formalism.

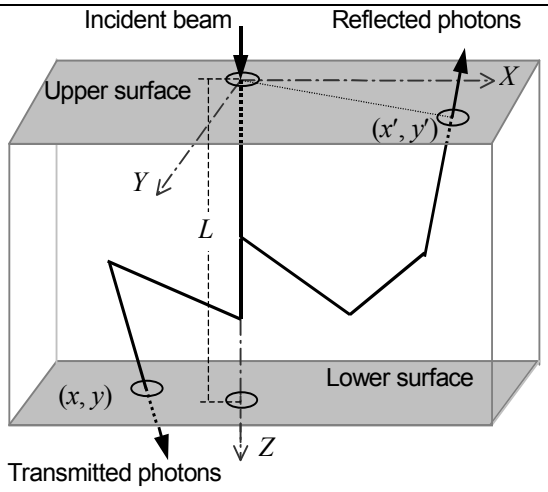

Fig. 24. Geometry of multiple-scattering events in a slab of turbid medium.

During the propagation of a photon packet, we use a single-scattering matrix $\mathbf{M}(\Theta)$ and a rotation matrix $\mathbf{R}(\phi)$ to change the Stokes vector of the photon packet after each single-scattering event. If the photon has been scattered *n* times before it exits the scattering medium, we express its Stokes vector $\mathbf{S}_{out}^{n}$ as

$$\mathbf{S}_{out}^{n}(x, y; \mu_s, \mu_a) = [\mu_s /(\mu_a + \mu_s)]^n \times \mathbf{R}(\phi_L)\mathbf{M}(\Theta_n)\mathbf{R}(\phi_n)...\mathbf{M}(\Theta_1)\mathbf{R}(\phi_1)\mathbf{S}_0, \quad (28)$$

where μ_s, μ_a are the scattering coefficient and the absorption coefficient, respectively; and (x, y) is a detection point in the laboratory coordinate system; $[\mu_s/(\mu_a+\mu_s)]^n$ denotes the remaining energy after the photon packet has been scattered n times; $\mathbf{R}(\phi_i)$ and $\mathbf{M}(\Theta_i)$ (i=1,2,…,n) are the rotation matrix and the single-scattering matrix for the i^{th} scattering event; $\mathbf{R}(\phi_L)$ transforms the Stokes vector of the photon packet in the local coordinate system back to the Stokes vector in the laboratory coordinate system before the photon packet is received by the detector.

2.4 Double-scattering approximation

It has been proved in previous literature that a double-scattering approximation can effectively emulate the spatial patterns of back-scattered light obtained from experiments. The geometry of a double-scattering event is shown in Fig. 25.

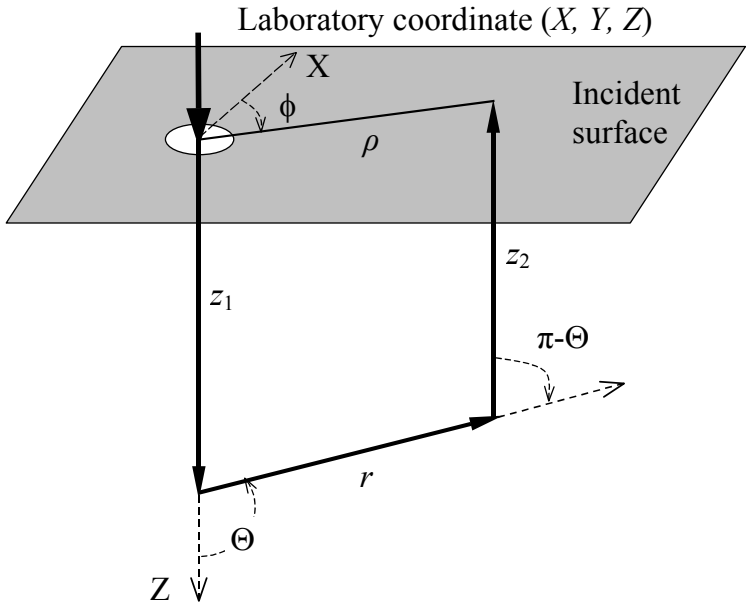

Fig. 25. Geometry of a double-scattering event in a slab of turbid medium.

Given the Stokes vector of the incident light $\mathbf{S}_0$, the Stokes vector of the backscattered light after double-scattering events $\mathbf{S}_2^{bs}$ can be expressed as

$$\mathbf{S}_2^{\mathrm{bs}}(\rho,\phi)=\mu_s^2\int_0^\infty\int_0^\infty\frac{dz_1dz_2}{r^2}\{\exp[-\mu_T(|z_1|+|z_2|+r)]\times\mathbf{R}(\phi)\mathbf{M}(\pi-\Theta)\mathbf{M}(\Theta)\mathbf{R}(\phi)\mathbf{S}_0\}. \quad (29)$$

In case of Rayleigh scattering, the single-scattering matrices $\mathbf{M}(\pi-\Theta)$ and $\mathbf{M}(\Theta)$ can be simply expressed as $\begin{bmatrix} a & b & 0 & 0 \\ b & a & 0 & 0 \\ 0 & 0 & d & 0 \\ 0 & 0 & 0 & d \end{bmatrix}$ and $\begin{bmatrix} a' & b' & 0 & 0 \\ b' & a' & 0 & 0 \\ 0 & 0 & d' & 0 \\ 0 & 0 & 0 & d' \end{bmatrix}$. The rotation matrix $\mathbf{R}(\phi)$ is shown in Eq. (14). Then the analytic expression of the back-scattering Mueller matrix based on the double-scattering approximation can be written as

$$\mathbf{M}=\begin{bmatrix} aa'+bb' & (ab'+ba')\cos 2\phi & (ab'+ba')\sin 2\phi & 0 \\ ba'\cos 2\phi & (bb'+aa')\cos^2 2\phi-dd'\sin^2 2\phi & (bb'+aa'+dd')\sin 2\phi\cos 2\phi & 0 \\ -ba'\sin 2\phi & (-bb'-aa'-dd')\cos 2\phi\sin 2\phi & (-bb'-aa')\sin^2 2\phi+dd'\cos^2 2\phi & 0 \\ 0 & 0 & 0 & dd' \end{bmatrix} \quad (30)$$

Please note that when observe the Mueller matrix patterns on the incident surface, the azimuthal angle ϕ has a clockwise rotation.

2.5 Scattering media with chiral material

As a chiral material, glucose has preferential handedness because it has an asymmetric molecular structure. Glucose interacts differently with right and left circular polarization states, resulting in the rotation of linearly polarized light.

The contribution of glucose during a free path between two adjacent scattering events can be expressed as a circular birefringence $\mathbf{R}(\theta)$:

$$\mathbf{R}(\theta)=\begin{bmatrix} 1 & 0 & 0 & 0 \\ 0 & \cos(2\theta) & -\sin(2\theta) & 0 \\ 0 & \sin(2\theta) & \cos(2\theta) & 0 \\ 0 & 0 & 0 & 1 \end{bmatrix}, \quad (31)$$

where θ denotes the optical rotation caused by glucose molecules, which is the product of the ORD (the specific rotation of glucose at a certain wavelength), the path length and the concentration of glucose.

2.6 Scattering media with birefringent effect

Until now, most theoretical studies about polarized light propagation in scattering media based on Monte Carlo simulation are limited to isotropic turbid media which do not possess birefringence. Birefringence is, however, prevalent in biological tissues, such as collagen or muscle. Tissue birefringence results primarily from the linear anisotropy of the fibrous structures that form the extra-cellular background medium. The refractive index of the background medium is higher along the length of fibers than that along the cross section. In birefringent turbid media, both birefringence and scattering alter the polarization of light. The anisotropic background refractive index around the scattering spheres may slightly change the distributions of the deflection angle Θ and the azimuthal angle ϕ. However, the birefringence value δ in biological tissue is quite weak (normally less than 1×10^{-2}), ignoring its perturbation on the PDF of Θ and ϕ is reasonable. Therefore, the birefringent effect on the polarization is only considered during the paths of light between scattering events.

A photon packet propagates a random distance s in a linearly birefringent turbid medium between two adjacent scattering events. The birefringent effect on the polarization state of the photon packet during this distance can be expressed by a linear retarder with two parameters, Δ and β, as shown in Eq. (32):

$$\mathbf{T}(\Delta,\beta)=\begin{bmatrix}1 & 0 & 0 & 0\\ 0 & C_4\sin^2(\Delta/2)+\cos^2(\Delta/2) & S_4\sin^2(\Delta/2) & -S_2\sin(\Delta)\\ 0 & S_4\sin^2(\Delta/2) & -C_4\sin^2(\Delta/2)+\cos^2(\Delta/2) & C_2\sin(\Delta)\\ 0 & S_2\sin(\Delta) & -C_2\sin(\Delta) & \cos(\Delta)\end{bmatrix},$$

$$\text{and } C_2=\cos(2\beta), C_4=\cos(4\beta), S_2=\sin(2\beta), S_4=\sin(4\beta), \tag{32}$$

where β is the azimuthal angle of the birefringent slow axis in the X-Y plane in the local coordinate of the propagating photon; Δ is the phase retardation, which can be expressed by

$$\Delta=(\Delta n)\times 2\pi s/\lambda, \tag{33}$$

where Δn is the difference between the maximum and minimum refractive indices in the plane perpendicular to the propagation orientation of the photon packet; and λ is the light

wavelength in the scattering medium. When the angle α between the slow axis of the medium and the propagation orientation of the photon packet is known,

$$\Delta n = n_s n_f \,/\, \sqrt{(n_s \cos\alpha)^2 + (n_f \sin\alpha)^2} - n_f , \tag{34}$$

where n_s and n_f are the refractive indices of the birefringent medium along the slow axis and the fast axis, respectively; the linear birefringence value δ is n_s–n_f.

On the double-scattering model and when the slow axis of the birefringence is along the X–axis, three linear retarders corresponding to the three steps, z_1, r and z_2, need to be considered. The parameters, Δ and β, in the first and the third retarders are

$$\Delta_1 = \delta \cdot \frac{2\pi z_1}{\lambda},\ \Delta_2 = \delta \cdot \frac{2\pi z_3}{\lambda},\ \beta_1 = \beta_3 = 0 . \tag{35}$$

The parameters Δ_2 and β_2 in the second retarder need to be deduced. After the first scattering event through an azimuthal angle ϕ and a deflection angle Θ, the local coordinate (X', Y', Z') can be expressed as

$$\begin{bmatrix} X' \\ Y' \\ Z' \end{bmatrix} = \begin{bmatrix} \cos\Theta\cos\phi & \cos\Theta\sin\phi & -\sin\Theta \\ -\sin\phi & \cos\phi & 0 \\ \sin\Theta\cos\phi & \sin\Theta\sin\phi & \cos\Theta \end{bmatrix} \begin{bmatrix} X \\ Y \\ Z \end{bmatrix} . \tag{36}$$

Then, there is no difficult to find that the azimuthal angle of the slow-axis (X-axis) on the X'–Y' plane can be expressed as

$$\beta_2 = \tan^{-1}\left(\frac{-\sin\phi}{\cos\Theta\cos\phi}\right) . \tag{37}$$

The phase retardation Δ_2 can be written as $\Delta_2 = \delta' \cdot \frac{2\pi r}{\lambda}$, where δ' is the difference between the maximum and the minimum refractive indices in the plane perpendicular to the propagation direction (Z'–axis) of the photon packet after the first scattering event. Since the angle between the slow-axis (X-axis) and the propagation direction (Z'–axis) is $\alpha = \cos^{-1}(\sin\Theta\cos\phi)$, then Δ_2 can be expressed as

$$\Delta_2 = \frac{2\pi r}{\lambda} \cdot \left(\frac{n_s n_f}{\sqrt{{n_s}^2 \cos^2\alpha + {n_f}^2 \sin^2\alpha}} - n_f \right) . \tag{38}$$

VITA

Xueding Wang received his B. S. in electronic science and engineering from Nanjing University in July 1997 and his M. S. in acoustics from Nanjing University in June 2000. He later researched under Dr. Lihong V. Wang of Texas A&M University from the fall of 2000. His research was mainly focused on the functional photoacoustic tomography (PAT) of animal brains—a novel non-invasive neuroimaging technology. He received his Ph.D. in biomedical engineering in August 2004.

C/O Xueding Wang
1515 Baltimore Dr.
Richardson, TX 75081
Tel. (972) 437-4959